Vilnius University
Physics Faculty
Laser Research Center

Alejandra Araceli Padilla Camargo

ABSORPTION SPECTROSCOPY WITH QUANTUM LIGHT

Master thesis

Laser Technologies study program
ICFO Institute of Photonic Sciences

Student	Alejandra Padilla
Supervisor	Prof. Juan P. Torres
Consultant	Dr. Vygandas Jarutis
Director of institute	Dr. Dalia Kaškelytė.

Vilnius 2023

This master's thesis project is the result of the collaboration between the *Quantum Engineering of Light* (QEL) group at ICFO-The Institute of Photonic Sciences (Barcelona, Spain) and the group of *Optical Communications* at the Department of Signal Theory and Communications (Universitat Politècnica de Catalunya, Barcelona, Spain). This collaboration involves Juan P. Torres (Group leader of QEL and professor at Universitat Politécnica de Catalunya), Daniel Urrego (PhD Student at ICFO), and Joan Gene (Visiting scientist at ICFO and professor with the Optical Communications group at Universitat Poliècnica de Catalunya). Professor Jose Antonio Lazaro is the scientist responsible at the Optical Communications group of this collaboration. We should mention that the Programmable optical filter at the optical communications frequency window (Waveshaper 1000s, Finisar), provided by the Optical Communications group, was a key element in the development of this Project, and we are especially thankful to Professor Lazaro and Professor Gene for this. We are also especially thankful to Daniel Urrego, who has made an enormous contribution to this Project, with his knowledge and experience generating and detecting single and paired photons.

Contents

1 Introduction

Absorption Spectroscopy: a tool for material analysis

When electromagnetic radiation interacts with a sample, the different frequencies that make up the input radiation (*input spectrum*) can be absorbed differently by the sample. Absorption spectroscopy refers to the measurement of the absorption of electromagnetic radiation as a function of frequency (*the absorption spectrum*). The beginning of absorption spectroscopy can be dated back to the beginning of the XIX century, to the works of William Hyde Wollaston, William Herschel, and Joseph Von Fraunhofer, to cite a few [1]. One of the first applications of absorption spectroscopy was to measure the absorption spectrum of light coming from the Sun. With the help of work developed by Gustav Kirchoff and Robert Bunsen, it was concluded that each chemical element absorbs electromagnetic radiation at discrete frequencies, being the distribution of these array of frequencies unique for each element [2]. As a consequence, the spectrum of light coming from the Sun shows what are the main chemical elements present at the Sun. At the beginning of the XX century, the invention of Quantum Mechanics gave a full explanation for this fact. The absorption spectrum is related to the particular distribution of energy levels of each chemical element, that is a unique fingerprint of each element.

Inspection of the absorption spectrum of a sample is a tool routinely used in many applications to determine specific aspects of its composition. Sometimes one is interested only in the degree of absorption of a few frequencies. This is the case of a pulse oximetry, aimed at measuring the oxygen saturation in the arterial blood that provides information on the adequacy of respiratory function [3]. The key enabling tool of pulse oximetry is the measurement of the degree of absorption of the oxygenated/deoxygenated hemoglobin molecules at two different wavelengths, where the difference in absorption can be most easily detected. From a technological point of view, a pulse oximeter requires two lasers that emit at the wavelengths chosen and optical detectors sensitive enough at the corresponding wavelengths.

When one is interested in measuring the absorption spectrum in a certain frequency range, several experimental schemes can work. For instance, one might use a laser with broadband emission in the frequency range of interest, and tunable filters that can select small regions of the spectrum. One robust and low-cost solution are *filter spectrometers* designed for the NIR mounted on a rotating wheel. The wheel has either a set of filters with predefined wavelength regions for a specific application or a set of filters for the region of interest [4]. This approach was used to characterize the optical properties of graphene prepared on top of Si wafers with a certain thickness of SiO_2 [5]. They used white light with 12 narrowband filters with bandwidth $\sim$ 10 nm that covered the wavelength range from 410 nm to 740 nm.

Instead of a broadband laser followed by narrowband filters, one can use a tunable laser that covers the same frequency range of interest. These *frequency swept* lasers periodically tune the optical wavelength of a laser source through a certain range, which can be a relatively large range of e.g. 100 nm or more. At the detection stage, one can measure the absorption spectrum by means of a spectrometer, which at its most fundamental, consists of a diffraction grating or a prism, that separates light into its wavelength components with certain resolution.

Technological limitations of Absorption Spectroscopy

With the development of new light sources, absorption spectroscopy techniques have expanded into new frequency bands. Absorption spectroscopy can be classified according to the frequency band considered: ultraviolet-visible (UV-VIS) from ~ 175 to ~ 750 nm, near-infrared (NIR) from 0.8 to 2.5 μm, mid-infrared (MIR) from 2.5 to 25 μm, and far-infrared (FIR) from 25 to 1000 μm [6]. Choosing one frequency band over others to characterize the chemical composition of a sample depends mainly on its electromagnetic response, what lasers can efficiently stimulate the molecular transitions of the chemical components that make the sample.

Although doing absorption spectroscopy at the optimum frequency band could be a valuable source of information about the sample, the technology available at this frequency band might seriously limit the capabilities of absorption spectroscopy. Important considerations might be the unavailability of robust, low-cost, or ready-to-use light sources at a specific frequency range, the need to use high-cost optical equipment, and the lack of appropriate optical elements (narrowband filters) and highly sensitive detectors. For instance, the mid and far infrared optical ranges might provide useful information for health diagnostics, environmental sensing, and material analysis [7]. However, if one requires detector sensitivity at the single-photon level, the most efficient single-photon counting modules are at around ~ 800 nm.

An important issue concerning the achievable resolution in absorption spectroscopy is the bandwidth limitation of narrowband filters at certain frequency bands, especially if one restricts to use commercially available optical equipment. For example, the narrowest low-cost spectral filter available commercially at ~ 810 nm has a bandwidth between 3 and 5 nm. For comparison, the best filters commercially available are designed for the frequency range corresponding to optical communications, i.e. ~ 1550 nm. In this frequency range, the need to separate optical channels to enhance transmission capacity has enabled the production of narrowband filters with bandwidths not easily available at other frequency bands. In the C band, from 1527 to 1567 nm, filters with bandwidths of 10 GHz, i.e., 0.08 nm at 1550 nm, are commercially available.

Quantum light: how advanced technology in one frequency band can assist absorption spectroscopy in another frequency band with inferior technology

In this Master thesis, we show that the use of quantum light allows us to overcome some of the technological limitations that prevent the application of absorption spectroscopy at certain frequency bands or degrade its performance because of limitations on the bandwidth of narrowband filters or the sensitivity of optical detectors. We consider two schemes. The first scheme makes use of frequency-entangled paired photons at different frequency bands and needs the measurement of coincidences between paired photons. The second scheme is based on the idea of quantum interference in a SU(1,1) interferometer and does not require the measurement of coincidences.

The first scheme that we will consider makes use of highly frequency-entangled signal/idler photon pairs generated via spontaneous parametric down-conversion (SPDC). The signal photons have frequency $\omega_s + \Omega$ and the idler photons have frequency $\omega_i - \Omega$, where $\omega_{s,i}$ are the central frequencies of signal/idler photons and Ω is the frequency deviation from the corresponding central frequency. Signal and idler photons are generated at different frequency bands. The high degree of entanglement is achieved by using a pump beam with a bandwidth ($\sim$ 5 MHz) much smaller than the bandwidth of the generated photon pairs. If we have optical technology that allows us to filter signal photons with a bandwidth $\Delta\lambda_s$, we will see that this translates into filtering the idler photons with bandwidth

$$\Delta\lambda_i = \left(\frac{\lambda_i}{\lambda_s}\right)^2 \Delta\lambda_s \tag{1}$$

where $\lambda_{s,i} = 2\pi c/\omega_{s,i}$ are the central wavelengths of the signal and idler photons. For instance, for signal and idler photons with central wavelengths, $\lambda_s = 1550$ nm and $\lambda_i = 810$ nm, filtering with a frequency resolution of $\Delta\lambda_s = 1$ nm at the signal photon frequency band translates into filtering with a frequency resolution of $\Delta\lambda_i = 0.27$ nm at the idler frequency band. This is one order of magnitude better than the bandwidth of commercially available spectral filters at 810 nm.

The scheme considered above allows us to *create* effective narrowband filters at one frequency band, overcoming technological limitations, by programming the filter at another frequency band. Notwithstanding, since the scheme makes use of coincidence measurements, we still need good optical detectors (sensitive enough) at both frequency bands. The second scheme considered avoids this limitation and allows doing absorption spectroscopy at the idler wavelength range without making any measurement at this wavelength. All measurements are made at the signal wavelength range where advanced technology exists. The key element of this

second scheme is a SU(1,1) interferometer, a Mach-Zehnder interferometer with two nonlinear crystals inside, where the nonlinear process of spontaneous parametric downconversion takes place at the first crystal, and parametric amplification takes place in the second nonlinear crystal.

Some previous works relevant to the topics considered in this Project

The first demonstration, to the best of our knowledge, of using the quantum correlations present in paired photons generated in spontaneous parametric down-conversion (SPDC) for spectroscopy was done in 2003 [8]. They used a 8 mm type II LBO crystal pumped at $\lambda_p = 457.9$ nm, which was slightly tilted for achieving non-collinear non-degenerate SPDC. They measured three frequency filters centered at $\lambda_s = 850$ nm (10 nm bandwidth), 885.6 nm (11 nm bandwidth), and 916 nm (12 nm bandwidth). For the measurements, in the frequency range around 916 nm, they used a monochromator with a frequency resolution of 2 nm. Notice that their measurements were very close to frequency degeneracy, indeed the last filter was measured at frequency degeneracy.

At the same time, following the same principles, Atsushi et al. [9] measured some of the peaks of the absorption spectrum of an Nd^{3+} doped glass (at 810 and 870 nm). They generated photon pairs by SPDC in a 1 mm thick type II BBO crystal pumped at $\lambda_p = 429.7$ nm. As in the case discussed above, the frequency range of signal and idler photons was very similar, the SPDC system is again close to frequency degeneracy.

In 2018, Kalachev et al. [10] published a paper titled *Biphoton spectroscopy in a strongly non-degenerate regime of SPDC*. The goal was to measure the absorption spectrum of Cr^{3+} ions in Al_2O_3 crystal. However, their experimental scheme is frequency degenerate type I collinear SPDC, using a 10 mm thick $LiIO_3$ crystal pumped by a He-Cd laser (325 nm). Maybe the confusion comes from the way that they define the *strongly non-degenerate regime* of SPDC: when the difference in frequencies of correlated photons exceeds significantly their spectral width. This is somehow different from the usual definition of non-degenerate SPDC when the frequency bands where signal-idler photons live are *really* different.

Slattery et al. [11] implemented in 2013 a truly non-degenerate SPDC source for spectroscopy based on quantum correlated photons. They used a collinear non-degenerate SPDC source that consisted of a 20 mm periodically-poled lithium niobate (PPLN) crystal, pumped at 532 nm and generating pairs of signal (central wavelength: 895 nm; bandwidth: 1.15 nm) and idler (central wavelength: 1310 nm; bandwidth: 2.5 nm wavelength) photons. As a filter, they used a volume Bragg grating with high reflection at 895 nm with a bandwidth smaller than 0.1 nm. Since they did not have an efficient single-photon counting module at the idler

frequency (1310 nm), for detection they sent the idler photon to a spectrally resolving tunable up-conversion detector system which is pumped by a strong 1550 nm laser and generates single photons at 710 nm, which can be efficiently detected with a single-photon counting module.

The work of Barreto et al. [12] in 2014 gave way to a renewed interest in new types of interferometers based on the concept of induced coherence [13, 14], and the use of new geometries [15]. Indeed, some authors [16], that include A. Zeilinger, one of the winners of the Nobel Prize in Physics 2022, talk of the *awakening of a sleeping beauty* referring to the present interest in a beautiful idea demonstrated at the beginning of the 1990s in Leonard Mandel's laboratory at Rochester University [13, 14]. Most of the new implementations were oriented towards applications in imaging [12], optical coherence tomography [17], and spectroscopy [18], to name a few. In this last case, Kalashnikov et al. demonstrated the feasibility of doing absorption spectroscopy of CO_2 gas at the frequency band around one of the absorption peaks of its spectrum (4.28μm), while measuring light at a frequency band around (608 nm). They made use of a nonlinear interferometer, that contains insider second-order nonlinear crystals pumped by a common laser at 532 nm.

This Project aims at going one step further following the scientific path initiated by some of the papers reviewed above. We want to stress the technological benefits of using quantum light for spectroscopy. We want to show a *real* example of how to make use of advanced filtering technology at one frequency band (Telecomm window around 1550 nm) to perform high-resolution frequency measurements at another frequency band. At the 810 nm frequency band, there is no such thing as the high-resolution Programmable optical filter (Waveshaper 1000s, Finisar) that we use here. In spite of this, we can benefit at 810 nm of this technology developed for the Telecomm window. Quantum correlations make possible the *frequency translation*.

We aim at obtaining simple results that can clearly show the possibilities offered by the two schemes consider for absorption spectroscopy. Even though we use quantum analysis in the Heisenberg picture, which can be sometimes cumbersome to use, and the meaning of its results difficult to grasp, we are able to obtain simple expressions in all cases and derive simple *recipes* for designing simple experimental implementations and interpreting the experimental results.

Finally, we want to highlight how the use of SU(1,1) interferometers for quantum spectroscopy is a step forward compared with the spectroscopy based on the use of *direct* quantum correlations between pairs of photons generated in SPDC. Although this last method, that was put forward some 20 years ago [8, 9], helped doing spectroscopy at one frequency band with less advanced technology available, it still has some drawbacks, as we will discuss in detail in Section 3.4, that can be overcome by using nonlinear interferometers.

Summary of the contents of this Project

In Chapter 2 we describe the process of parametric down-conversion (PDC), which is a key element of the two schemes that we present. We will do the quantum analysis of PDC in the Heisenberg picture. Although the quantum analysis of PDC is often done in the Schrodinger picture, where a first-order approximation is used to obtain the quantum state of signal/idler photons, the Heisenberg approach is more versatile and allows to analyze many different regimes of interest. The Schrodinger picture is most of the time considered in combination with a first-order approximation (also called low-parametric gain regime) since the treatment of the high-parametric gain regime is highly cumbersome in the Schrodinger picture.

In Chapter 3 we analyze the first scheme considered, based on the use of frequency-entangled photon pairs and coincidence measurements. After a detailed quantum analysis that makes use of the Heisenberg picture, we will describe the experimental setup used to make *proof of concept* experiments with this scheme. The spectral bandwidth of a filter centered at 810 nm would be measured using a programmable filter working at the Telecomm frequency band, around 1550 nm. This device can easily generate filters with a bandwidth of 0.01 nm. We will also show the results of experiments with spectral filters with an arbitrary shape, designed using the programmable filter at 1550 nm. Its spectral shape will be measured using a monochromator working at 810 nm.

In chapter 4 we analyze the second scheme considered: a SU(1,1) interferometer. We derive the main expressions and results with a detailed quantum analysis done in the Heisenberg picture. We present simulations that demonstrate the feasibility of this second approach.

In Chapter 5 we discuss the main aspects of the results obtained, and summarize the main conclusions of this Project, with special emphasis on comparing the two schemes considered here, what are the advantages/disadvantages of each one.

In Chapter 6, we briefly summarize the main results obtained in the framework of this Project.

2 Quantum analysis of Parametric down-conversion (PDC)

The two schemes presented above make use of the nonlinear process of parametric down-conversion (PDC) [19, 20]. In this nonlinear process, the presence of electric fields in a crystal induces a nonlinear polarization that can be written as [21]

$$\mathbf{P} = \epsilon_0 \chi^{(1)} \mathbf{E} + \epsilon_0 \chi^{(2)} \mathbf{E}^2 \tag{2}$$

The fact that the nonlinear polarization depends in a nonlinear way on the total electric field $\mathbf{E}$ is what allows the crystal to be referred to as a *nonlinear crystal*. The constant ϵ_0 is the vacuum permittivity, $\chi^{(1)}$ is the linear susceptibility and $\chi^{(2)}$ is the second-order nonlinear susceptibility. Although in most applications, the geometry of the problem makes it possible to consider the susceptibilities $\chi^{(1)}$ and $\chi^{(2)}$ as single numbers, we should remember that they constitute matrices indeed. The linear susceptibility $\chi^{(1)}$ is in general a 3×3 matrix and the second-order nonlinear susceptibility is a 3×6 matrix [22].

In PDC, there are three waves propagating inside the nonlinear crystal: the pump, signal, and idler waves. We consider a second-order nonlinear crystal such as $LiNbO_3$ (LN) in a non-degenerate, collinear, type 0 configuration, under the monochromatic undepleted pump beam approximation. More specifically, all this means that:

- **Non-degenerate**: All waves (pump, signal, and idler) have different frequencies. If we designate by ω_p, ω_s and ω_i the central frequencies of each wave, from the conservation of energy among all waves one could find that $\omega_p = \omega_s + \omega_i$ [19], or alternatively, in terms of the corresponding central wavelengths, $1/\lambda_p = 1/\lambda_s + 1/\lambda_i$. We will consider the case of $\lambda_p = 532$ nm, $\lambda_s = 1550$ nm and $\lambda_i = 810$ nm.

- **Collinear**: All waves propagate along the same direction inside the nonlinear crystal, which we designate as the spatial coordinate z. To separate the beams after leaving the nonlinear crystal we will make use of dichroic mirrors.

- **Type 0**: All waves have the same polarization. This has important consequences for the election and design of the nonlinear crystal. Besides the need of transparency in the frequency range of interest and a large nonlinear susceptibility to enhance the photon flux generated at PDC, the suitability of a nonlinear crystal for PDC depends on the capacity to achieve the phase matching condition, that all waves generated inside the nonlinear crystal add coherently after leaving the nonlinear crystal. The phase matching condition depends on many characteristics of the crystal such as wavelength range considered, refractive index, temperature, and mechanical properties, to cite a few [23]. In the case of type 0 PDC, we need to use quasi-phase-matching (QPM) [19, 21]. QPM is implemented by a periodic modulation of the nonlinear susceptibility of the material along z with

period $\Lambda = \pi/\Delta k$, where $\Delta k = k_p - k_s - k_i$ and $k_{p,s,i}$ are the wavenumbers of the pump, signal, and idler waves, respectively. In Lithium Niobate (LN), this is done by periodically reversing its ferroelectric domain polarity. A material fabricated in this way is referred to as periodically poled LN (PPLN).

- **Undepleted pump beam approximation**: The pump beam is a classical intense beam generated by a laser. In most applications, the pump power can go from a few mW to $1-2$ W. On the contrary, the flux rate of down-converted photons generated (signal and idler waves) is very small compared with the flux rate of pump photons, so we can assume that the energy of the pump beam is unchanged in the PDC process (pump beam undepleted approximation).

- **Monochromatic pump beam**: The bandwidth of the pump beam is much smaller than the bandwidth of the signal and idler waves. In our case, the pump beam is CW (quasi-monochromatic wave generated by a Verdi laser with central wavelength 532 nm and bandwidth $\sim$ 5 MHz). The bandwidth of signal and idler waves is much bigger (we will see in Chapter 3 that is several nanometers wide). We can safely assume that the pump beam is monochromatic with frequency ω_p. In this case, the signal and idler photons show frequency anti-correlation, i.e., if the frequency of the signal photon is $\omega_s + \Omega$, and the frequency of the companion idler photon is $\omega_i - \Omega$.

The quantum description of parametric down-conversion (PDC) is done in terms of continuous field operators [24–26].

The general scheme of PDC in a quantum language is shown in Fig. (1). An intense monochromatic pump beam E_p with frequency ω_p illuminates the nonlinear crystal. b_s and b_i designate the quantum operators associated to the signal (central frequency ω_s) and idler (ω_i) waves at the input face of the nonlinear crystal. a_s and a_i designate the corresponding quantum operators at the output face of the nonlinear crystal. In [20] one can find a detailed derivation of how to quantize the classical evolution equations that describe the nonlinear process of PDC under the paraxial approximation [19]. When the input quantum state of signal/idler waves is the vacuum state, we talk about spontaneous parametric down-conversion (SPDC). This is the case that we will consider in Chapter 3. If the signal or idler quantum states are not the vacuum, we talk about optical parametric amplification (OPA). In Chapter 4 we will consider a SU(1,1) interferometer where all waves pass through a second-order nonlinear crystal twice. The first pass by the nonlinear crystal can be described as SPDC, while the second pass by the nonlinear crystal constitutes OPA.

In most situations of interest, that include the cases we consider in this project, the spatial bandwidth in the transverse wavenumber domain $\mathbf{q}$ is much bigger than the spatial bandwidth of the pump beam. This is the case when the diffraction length of the pump beam $L_{dif} = k_p w_p^2$,

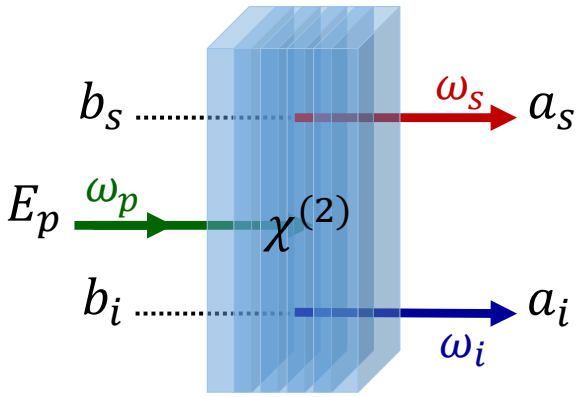

Figure. 1 Sketch of the waves involved in parametric down-conversion (PDC) in a quantum formalism. An intense pump beam E_p with frequency ω_p illuminates a $\chi^{(2)}$ nonlinear medium (nonlinear crystal) and mediates the generation of paired photons: signal (central frequency ω_s) and idler (central frequency ω_i). $b_{s,i}$ are the input quantum operators associated to the signal and idler modes, and $a_{s,i}$ are the output quantum operators for the signal and idler modes.

where w_p is the pump beam waist, and the diffraction lengths associated to the detection modes, $L_{s,i} = k_{s,i} w_{s,i}^2$, is much larger than the nonlinear crystal length L. $k_{p,s,i}$ are the wavenumbers of all waves involved. The plane wave approximation would correspond to considering that the pump beam is effectively a plane wave. For the first scheme considered (see Chapter 3), we do not consider the plane wave approximation in order to take into account the effects of having a finite focused pump beam on the flux rates of down-converted photons. In Chapter 4 we will make use of the plane wave approximation.

Under these conditions and approximations, we can write the relationship between the input quantum operators b_s and b_i, and the output quantum operators a_s and a_i as Bogoliuvov relationships [27]

$$
\begin{aligned}
a_s(\Omega, \mathbf{q}) &= U_s(\Omega, \mathbf{q})\, b_s(\Omega, \mathbf{q}) + \frac{V_s(\Omega, \mathbf{q})}{(2\pi)\, I_p^{1/2}} \int d\mathbf{q}_p\, E_p(\mathbf{q}_p)\, b_i^\dagger(-\Omega, \mathbf{q}_p - \mathbf{q}), \\
a_i(\Omega, \mathbf{q}) &= U_i(\Omega, \mathbf{q})\, b_i(\Omega, \mathbf{q}) + \frac{V_i(\Omega, \mathbf{q})}{(2\pi)\, I_p^{1/2}} \int d\mathbf{q}_p E_p(\mathbf{q}_p)\, b_s^\dagger(-\Omega, \mathbf{q}_p - \mathbf{q}),
\end{aligned}
\tag{3}
$$

where I_p is the average flux density of pump beam photons, i.e., $I_p = N_p/S_p$, N_p is the total number of pump photons and $S_p = W_p^2$ is the area of the pump beam. $\mathbf{q}_p$ designates the transverse wavenumber of the pump beam. $E_p(\mathbf{q}_p)$ is normalized so that $\int d\mathbf{q}_p\, |E_p(\mathbf{q}_p)|^2 = N_p$. One can recover the Bogouliuvov relationships for the plane pump beam approximation by substituting $E_p\,(\Omega_p, \mathbf{q}_p) = (2\pi)\, I_p^{1/2} \delta(\mathbf{q}_p)$ into Eq. (3).

The functions $U_{s,i}$ and $V_{s,i}$ are [20, 28–30]

$$U_{s,i}(\Omega) = \left\{\cosh(\Gamma_{s,i}L) - i\frac{\Delta_{s,i}}{2\Gamma_{s,i}}\sinh(\Gamma_{s,i}L)\right\}\exp\left\{i\left[k_p^0 + k_{s,i}(\Omega,\mathbf{q}) - k_{i,s}(-\Omega,-\mathbf{q})\right]\frac{L}{2}\right\},$$
$$V_{s,i}(\Omega) = -i(\sigma L)\frac{\sinh(\Gamma_{s,i}L)}{\Gamma_{s,i}L}\exp\left\{i\left[k_p^0 + k_{s,i}(\Omega,\mathbf{q}) - k_{i,s}(-\Omega,-\mathbf{q})\right]\frac{L}{2} + i\varphi_p\right\}. \quad (4)$$

$k_{p,s,i}$ are the wavenumbers of all waves involved, $\Gamma_{s,i} = [\sigma^2 - \Delta_{s,i}^2/4]^{1/2}$, and L is the crystal length. The nonlinear coefficient σ (units of m^{-1}) is

$$\sigma = \left(\frac{\hbar\omega_p\omega_s\omega_i[\chi^{(2)}]^2 F_p}{8\epsilon_0 c^3 n_p n_s n_i}\right)^{1/2}, \quad (5)$$

$n_{s,i,p}$ are refractive indexes, $\chi^{(2)}$ is the second-order nonlinear coefficient of the crystal and F_p is the flux rate of pump photons (photons/s/m^2). The parameter $G = \sigma L$ is the gain of the parametric down-conversion process, that determines the strength of the PDC process, and therefore in what regime we are: low or high parametric gain. φ_p is the phase of the pump beam. The phase mismatch function is

$$\Delta = \Delta_s = -\Delta_i = k_p^0 - k_{s,i}(\Omega) - k_{i,s}(-\Omega) = (D_i - D_s)\Omega - \left(\frac{1}{2k_s} + \frac{1}{2k_i}\right)|\mathbf{q}|^2, \quad (6)$$

where $D_{s,i}$ are inverse group velocities (measured in s/m).

One important case is the low parametric gain regime ($G \ll 1$, our case in Chapter 3), which is the situation in most experimental implementations of SPDC. We can write [20]

$$U_{s,i}(\Omega) = \exp\left[ik_{s,i}(\Omega,\mathbf{q})\,L\right]$$
$$V_{s,i}(\Omega) = -i(\sigma L)\mathrm{sinc}\left[\frac{\Delta L}{2}\right]\exp\left\{i\left[k_p^0 + k_{s,i}(\Omega,\mathbf{q}) - k_{i,s}(-\Omega,-\mathbf{q})\right]\frac{L}{2} + i\varphi_p\right\}. \quad (7)$$

Alternatively, we can obtain the Bogoliuvov relationships in Eq. (7) by making an expansion of the general Bogoliuvov relationships to first order in the nonlinear coefficient σ [31].

3 Quantum spectroscopy based on coincidence measurements of frequency-entangled photon pairs

We want to measure the unknown spectral shape of a frequency filter $H_i(\omega_i + \Omega)$ at the frequency band of the idler photon. The idler photons are reflected, or transmitted, by the frequency filter. Since the frequency of signal and idler photons are anti-correlated, if we make use, in the signal path, of a narrowband frequency filter with bandwidth $\Delta\Omega_s$ and central frequency Δ_s, the probability P_{si} to detect an idler photon in coincidence with a signal photon will be

$$P_{si} \propto |H_i(\omega_i - \Delta_s)|^2 \, \Delta\Omega_s. \tag{8}$$

If we use different values of Δ_s, we can recover the spectral shape of $|H_i(\omega_i + \Omega)|^2$ by using tunable filters at the signal frequency band, without the need to use filters at the idler frequency.

The frequency anti-correlation between signal and idler photons imposes $\Delta\Omega_s = -\Delta\Omega_i$. If we make use of the relationship $\Delta\lambda = (2\pi c/\lambda^2)\,\Delta\Omega$, that is valid for small values of the bandwidth, the wavelength resolution at the idler frequency band is

$$\Delta\lambda_i = \left(\frac{\lambda_i}{\lambda_s}\right)^2 \Delta\lambda_s. \tag{9}$$

Equation (9) shows that we can take advantage of advanced technology that can build extremely narrowband frequency filters at the signal frequency band to create equally extreme narrowband filters at the idler frequency band. In this sense, the use of quantum correlations between signal/idler photons allows to expand the applicability of a technology (narrowband filtering at the telecom frequency band) beyond the frequency range for which it was designed.

3.1 Theoretical calculation of the expected flux rates for singles (signal or idler photons alone) and signal/idler coincidences

Quantum description of the detection system

On the detection stage, signal and idler photons are projected onto spatial modes with a Gaussian shape with beam waist w_s [$F_s(\mathbf{x})$ and $F_i(\mathbf{x})$], with the help of imaging systems and single-mode fibers. The quantum operator that describes this projection operation is

$$\mathcal{A}_s(t) = \int d\mathbf{x}\, A_s(\mathbf{x}, t) F_s^*(\mathbf{x}), \tag{10}$$

where $A(\mathbf{x}, t)$ is the quantum operator that describes signal photons in coordinate space. Similarly for the idler photons. If we make use of the Fourier transform relationship between

quantum operators and functions

$$A_s(\mathbf{x},t) = \frac{1}{(2\pi)^{3/2}} \int d\Omega\, d\mathbf{q}\, a_s(\Omega,\mathbf{q})\, \exp\left(-i\Omega t + i\mathbf{q}\cdot\mathbf{x}\right),$$
$$F_s(\mathbf{x}) = \frac{1}{(2\pi)} \int d\mathbf{q}\, F_s(\mathbf{q})\, \exp\left(i\mathbf{q}\cdot\mathbf{x}\right), \tag{11}$$

we obtain that the projection operator is

$$\mathcal{A}_s(t) = \frac{1}{(2\pi)^{1/2}} \int d\Omega\, d\mathbf{q}\, a_s(\mathbf{q},\Omega) F_s^*(\mathbf{q}) \exp(-i\Omega t). \tag{12}$$

To derive Eq. (12) we have made use of the identity

$$\int d\mathbf{x}\, \exp\left[i\left(\mathbf{q}_1 - \mathbf{q}_2\right]\cdot\mathbf{x}\right) = (2\pi)^2 \delta(\mathbf{q}_1 - \mathbf{q}_2). \tag{13}$$

Transformation of quantum operators under the presence of losses

Signal and idler photons, generated in SPDC, are transmitted (or reflected) from frequency filters located in signal/idler paths, that introduce frequency-dependent losses that the quantum formalism should take into account [32]. The frequency filter in the idler path has an unknown spectral shape that we want to measure. For the sake of simplicity, we also include in the expression of the filters the losses that the photons suffer when they traverse the corresponding optical systems. We assume that these losses are frequency independent in the bandwidth of interest, to avoid any external distorsion of the measurement of the spectral shape of filters. The transformations of the signal and idler quantum operators due to the presence of frequency filters and losses are [32]

$$a_s(\omega_s + \Omega) \longrightarrow H_s(\omega_s + \Omega)\, a_s + L_s(\omega_s + \Omega),$$
$$a_i(\omega_i + \Omega) \longrightarrow H_i(\omega_i + \Omega)\, a_i + L_i(\omega_i + \Omega), \tag{14}$$

where the operator L_s and L_i fulfill the commutation relationships

$$\left[L_i(\omega_i + \Omega), L_i^\dagger(\omega_i + \Omega')\right] = \left[1 - |H_s(\omega_i + \Omega)|^2\right] \delta\left(\Omega - \Omega'\right),$$
$$\left[L_s(\omega_s + \Omega), L_s^\dagger(\omega_s + \Omega')\right] = \left[1 - |H_s(\omega_s + \Omega)|^2\right] \delta\left(\Omega - \Omega'\right). \tag{15}$$

Flux rate of signal photons

The signal photons are transmitted (or reflected) through a tunable filter with central frequency Ω_0 and narrow bandwidth B_s. The number of signal photons $R_1(\Omega_0)$ detected per second is

$$R_1(\Omega_0) = \langle \mathcal{A}_s^\dagger(t)\mathcal{A}_s(t)\rangle = \frac{1}{2\pi}\,\frac{1}{(2\pi)^2}\frac{1}{I_p}\int d\Omega_1\, d\Omega_2\, d\mathbf{q}_1\, d\mathbf{q}_2\, \exp\left[i(\Omega_1-\Omega_2)t\right]$$
$$\times V_s^*(\Omega_1,\mathbf{q}_1)\, V_s(\Omega_2,\mathbf{q}_2) F_s(\mathbf{q}_1)\, F_s^*(\mathbf{q}_2) H_s(\Omega_0+\Omega_1) H_s^*(\Omega_0+\Omega_2)$$
$$\times \int d\mathbf{q}_p\, d\mathbf{q}_p'\, E_p^*(\mathbf{q}_p) E_p(\mathbf{q}_p')\, \langle b_i(-\Omega_1,\mathbf{q}_p-\mathbf{q}_1)\, b_i^\dagger(-\Omega_2,\mathbf{q}_p'-\mathbf{q}_2)\rangle. \tag{16}$$

For the sake of simplicity, we have written only the terms that will give a non-zero contribution to the flux rate. The pump beam and projections modes are normalized, so they can be written as

$$E_p(\mathbf{q}) = N_p^{1/2}\,\frac{w_p}{\pi}\exp\left(-\frac{|\mathbf{q}|^2\, w_p^2}{2\pi}\right), \tag{17}$$

and

$$F_s(\mathbf{q}) = \frac{w_s}{\pi}\exp\left(-\frac{|\mathbf{q}|^2\, w_s^2}{2\pi}\right). \tag{18}$$

If we make use of the commutation relationships

$$[b_i(\Omega_1,\mathbf{q}_1),\, b_i^\dagger(\Omega_2,\mathbf{q}_2)] = \delta(\Omega_1-\Omega_2,\mathbf{q}_1-\mathbf{q}_2), \tag{19}$$

and we make the integral over the variable $\mathbf{q}_p$,

$$\int d\mathbf{q}_p\, E_p^*(\mathbf{q}_p) E_p(\mathbf{q}_p+\mathbf{q}_2-\mathbf{q}_1) = N_p\,\exp\left(-\frac{|\mathbf{q}_1-\mathbf{q}_2|^2\, w_p^2}{4\pi}\right), \tag{20}$$

we can write

$$R_1(\Omega_0) = \frac{1}{2\pi}\,\frac{1}{(2\pi)^2}\frac{N_p}{I_p}\int d\Omega\, d\mathbf{q}_1\, d\mathbf{q}_2\, V_s^*(\Omega,\mathbf{q}_1)\, V_s(\Omega,\mathbf{q}_2)|H_s(\Omega_0+\Omega)|^2$$
$$\times F_s(\mathbf{q}_1)\, F_s^*(\mathbf{q}_2)\exp\left(-\frac{|\mathbf{q}_1-\mathbf{q}_2|^2\, w_p^2}{4\pi}\right). \tag{21}$$

If we assume that the V_s function is constant for the range of Ω and $\mathbf{q}$ where the projection modes and frequency filters are non-negligible, we can write

$$R_1(\Omega_0) = \frac{\sinh^2 G}{(2\pi)^3} B_s \, |V_s(-\Omega_0)|^2 \frac{w_p^2 w_s^2}{\pi^2} \int d\mathbf{q}_1 \, d\mathbf{q}_2 \, \exp\left(-\frac{|\mathbf{q}_1|^2 w_s^2}{2\pi} - \frac{|\mathbf{q}_2|^2 w_s^2}{2\pi} - \frac{|\mathbf{q}_1 - \mathbf{q}_2|^2 w_p^2}{4\pi} \right)$$
$$= \frac{\sinh^2 G}{(2\pi)^3} B_s \, |V_s(-\Omega_0)|^2 \, \frac{w_p^2 w_s^2}{\pi^2} \frac{1}{4} \frac{4\pi^2}{w_s^2} \, \frac{4\pi^2}{w_p^2 + w_s^2}, \tag{22}$$

where $G = \sigma L$ is the gain of PDC. After some straightforward simplifications, we can write that the number of signal photons detected per second $R_1(\Omega_0)$ is

$$R_1(\Omega_0) = \frac{\sinh^2 G}{2\pi} B_s \, |V_s(-\Omega_0)|^2 \, \frac{w_p^2}{w_p^2 + w_s^2}. \tag{23}$$

B_s is the bandwidth of the frequency filter in the signal path, w_p is the beam waist of the pump beam, and w_s is the beam width of the projection modes. For $w_p \gg w_s$, we recover the result of the plane wave approximation. Notice that the central frequency Ω_0 of the filter H_s is scanned, so the flux rate $R_1(\Omega_0)$ depends on the value of Ω_0.

Similarly, we can derive for the idler

$$R_2 = \frac{\sinh^2 G}{2\pi} B_i \, \frac{w_p^2}{w_p^2 + w_s^2}. \tag{24}$$

In the low parametric gain regime, we can approximate $\sinh^2 G \sim G^2 = (\sigma L)^2$.

Flux rate of signal/idler coincidences

We designate the window of coincidences as T_d. The number of signal-idler coincidences per second (R_{12}) is [33, 34]

$$R_{12} = \int_{T_d} d\tau \, \langle \mathcal{A}_s^\dagger(t) \mathcal{A}_i^\dagger(t+\tau) \mathcal{A}_i(t+\tau) \mathcal{A}_s(t) \rangle = R_1 R_2 T_d$$
$$+ \frac{1}{(2\pi)^4} \frac{1}{I_p} \int_{T_d} d\tau \int d\Omega_1 \, d\Omega_2 \, \exp\left[-i(\Omega_1 - \Omega_2)\tau\right] \, H_s^*(\Omega_1) H_i^*(-\Omega_1) \, H_s(\Omega_2) H_i(-\Omega_2)$$
$$\times \left| \int d\mathbf{q}_1 \, d\mathbf{q}_2 V_s^*(\Omega_1, \mathbf{q}_1) U_i^*(-\Omega_1, \mathbf{q}_2) F_s(\mathbf{q}_1) F_i(\mathbf{q}_2) \, E_p^*(\mathbf{q}_1 + \mathbf{q}_2) \right|^2. \tag{25}$$

Let us make the integral over τ. We have

$$\int_{T_d} d\tau \;\; \exp\left[-i(\Omega_1 - \Omega_2)\tau\right] = T_d \exp\left[-i \, (\Omega_1 - \Omega_2) \, \frac{T_d}{2} \right] \, \mathrm{sinc}\left[\frac{(\Omega_1 - \Omega_2) T_d}{2} \right]. \tag{26}$$

In the low parametric gain regime, we have (we restrict our attention to the frequency degree of freedom)

$$
\begin{aligned}
V_s(\Omega_1)U_i(-\Omega_1) &= \sigma L \,\mathrm{sinc}\left[\frac{D\Omega L}{2}\right] \exp\left\{i\left[k_p^0 + k_s(\Omega_1) - k_i(-\Omega_1)\right]\frac{L}{2} + ik_i(-\Omega_1)L\right\} \\
&= \sigma L \,\mathrm{sinc}\left[\frac{D\Omega L}{2}\right] \exp\left\{ik_p^0\frac{L}{2} + \left[k_s(\Omega_1) + k_i(-\Omega_1)\right]\frac{L}{2}\right\} \\
&= \sigma L \,\mathrm{sinc}\left[\frac{D\Omega L}{2}\right] \exp\left\{i\left[k_p^0 + k_s^0 + k_i^0\right]\frac{L}{2} + \left[\frac{1}{v_s} - \frac{1}{v_i}\right]\frac{L}{2}\Omega_1\right\},
\end{aligned}
\tag{27}
$$

where $v_{s,i}$ are group velocities of signal and idler photons. We need to calculate:

$$
\int d\Omega_1 d\Omega_2 \, T_d \mathrm{sinc}\left[\frac{(\Omega_1 - \Omega_2)T_d}{2}\right] \exp\left\{-i\frac{\Omega_1 - \Omega_2}{2}\left[T_d + \left(\frac{1}{v_s} - \frac{1}{v_i}\right)L\right]\right\}, \tag{28}
$$

To solve this we will make use of (see page 431, Eq. 3. 741, 2 in [35])

$$
\int_0^\infty dx \, \frac{sin(ax)\, cos(bx)}{x} = \begin{array}{ll} \frac{\pi}{2} & a > b \\ \frac{\pi}{4} & a = b \\ 0 & a < b \end{array} \tag{29}
$$

Here

$$
a = \frac{T_d}{2}, \qquad b = \frac{1}{2}\left[T_d + \left(\frac{1}{v_s} - \frac{1}{v_i}\right)L\right]. \tag{30}
$$

This implies that there are coincidences if

$$
a > b \longrightarrow \frac{1}{v_s} < \frac{1}{v_i} \longrightarrow v_s > v_i, \tag{31}
$$

and no coincidences if $v_s < v_i$. Indeed this is what we assume when we look for coincidences between a signal photon at time t with an idler photon at time $t + \tau$ ($\tau > 0$).

If $1/T_d$ is much larger than all bandwidths involved (SPDC, filters), we can substitute

$$
\mathrm{sinc}\left[\frac{(\Omega_1 - \Omega_2)T_d}{2}\right] \exp\left\{-i\frac{\Omega_1 - \Omega_2}{2}\left[T_d + \left(\frac{1}{v_s} - \frac{1}{v_i}\right)L\right]\right\} \longrightarrow \frac{2\pi}{T_d}\,\delta(\Omega_1 - \Omega_2), \tag{32}
$$

and obtain

$$
\begin{aligned}
R_{12} = R_1 R_2 T_d + \frac{(\sigma L)^2}{(2\pi)^3}\frac{1}{I_p}\int d\Omega \, |H_s(\Omega)|^2 |H_i(\Omega_0 + \Omega)|^2 |V(\Omega)|^2 \\
\left|\int d\mathbf{q}_1 \, d\mathbf{q}_2 F_s(\mathbf{q}_1) F_i(\mathbf{q}_2) \, E_p^*(\mathbf{q}_1 + \mathbf{q}_2)\right|^2 .
\end{aligned}
\tag{33}
$$

We do the integral over the spatial variables $\mathbf{q}_1$ and $\mathbf{q}_2$ and obtain

$$\int d\mathbf{q}_1\, d\mathbf{q}_2 F_s(\mathbf{q}_1) F_i(\mathbf{q}_2)\, E_p^*(\mathbf{q}_1+\mathbf{q}_2) = \frac{N_p^{1/2}}{4}\,\frac{w_s^2}{\pi^2}\,\frac{w_p}{\pi}\int d\mathbf{q}_-\exp\left[-\frac{|\mathbf{q}_-|^2 w_s^2}{4\pi}\right] \tag{34}$$
$$\times\int d\mathbf{q}_+\exp\left[-\frac{|\mathbf{q}_+|^2 w_s^2}{4\pi}-\frac{|\mathbf{q}_+|^2 w_p^2}{2\pi}\right] = \frac{N_p^{1/2}}{4}\,\frac{w_s^2}{\pi^2}\,\frac{w_p}{\pi}\,\frac{4\pi^2}{w_s^2}\,\frac{4\pi^2}{w_s^2+2w_p^2} = \frac{4\pi w_p N_p^{1/2}}{w_s^2+2w_p^2}.$$

The flux rate of signal/idler coincidences R_{12} is

$$R_{12}(\Omega_0) = R_1 R_2 T_d + \frac{(\sigma L)^2}{(2\pi)^3}\,\frac{16\pi^2 w_p^4}{(w_s^2+2w_p^2)^2}|H_s(-\Omega_0)|^2 B_i \mathrm{sinc}^2\left[\frac{DL\Omega_0}{2}\right] \tag{35}$$
$$= R_1 R_2 T_d + \frac{(\sigma L)^2}{2\pi}\,\frac{4w_p^4}{(2w_p^2+w_s^2)^2}|H_s(-\Omega_0)|^2 B_i \mathrm{sinc}^2\left[\frac{DL\Omega_0}{2}\right]. \tag{36}$$

Summary of main results

If we use a tunable filter in the signal path with central frequency Ω_0 and narrow bandwidth B_s to unveil the spectral shape of an unknown frequency filter in the idler path with effective bandwidth B_i, the flux rate of singles measurements (photons/s) are

$$R_1(\Omega_0) = \frac{(\sigma L)^2}{2\pi}\, B_s\, |V_s(-\Omega_0)|^2\,\frac{w_p^2}{w_p^2+w_s^2}, \tag{37}$$

for signal photons and

$$R_2 = \frac{(\sigma L)^2}{2\pi}\, B_i\,\frac{w_p^2}{w_p^2+w_s^2}, \tag{38}$$

for the idler photons.

The flux rate of coincidence measurements (coincidences/s) is

$$R_{12}(\Omega_0) = R_1(\Omega_0) R_2 T_d + \frac{(\sigma L)^2}{2\pi}\,\frac{4w_p^4}{(2w_p^2+w_s^2)^2}|H_s(-\Omega_0)|^2 B_i \mathrm{sinc}^2\left[\frac{DL\Omega_0}{2}\right]. \tag{39}$$

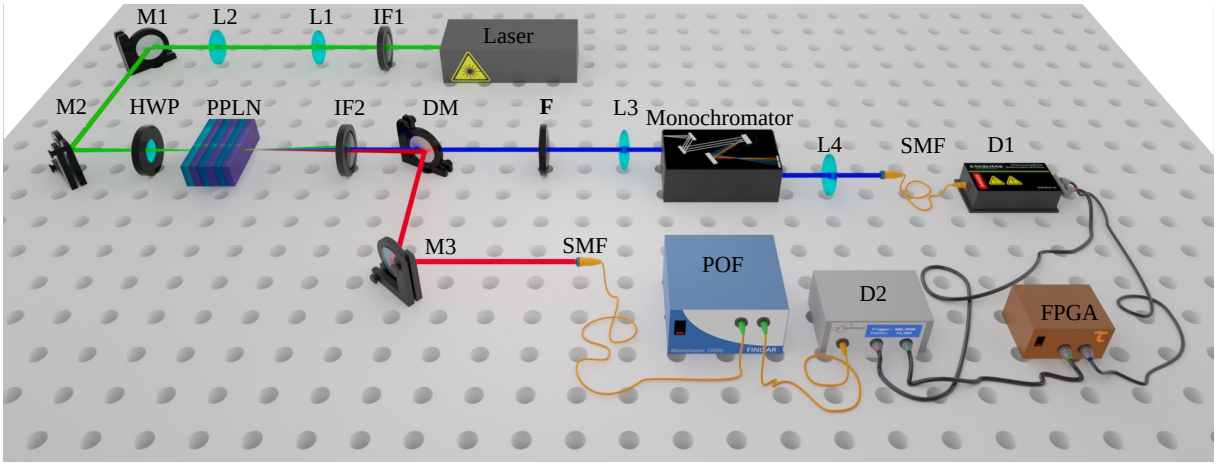

Figure. 2 Experimental setup. $IF_{1,2}$: interference filters, $L_{1,2,3,4}$: lenses, $M_{1,2,3}$: mirrors, HWP: half-wave plate, PPLN: periodically-poled lithium niobate crystal, DM: dichroic mirror, **F**: filter studied in the first part of the experiment, SMF: single-mode fibers, POF: Programmable optical filter, $D_{1,2}$ = Photon detectors, FPGA: counting module.

3.2 Experimental setup

The experimental setup for demonstrating quantum spectroscopy based on coincidence measurements is shown in Fig. 2. The pump beam is a Verdi V-10 diode-pumped laser (Coherent) with an emission wavelength of $\lambda_p = 532$ nm. A single-band bandpass filter (IF1) with a center wavelength of 532 nm (Brightline) is used to block residual emission from the Verdi laser. This is needed due to the laser's operating principle. Namely, the Verdi laser is composed of two diodes with emission wavelength at 808 nm that pump a Neodymium Vanadate (Nd:YVO_4) crystal, which emits light at 1064 nm. This light is then frequency-doubled by an LBO crystal in a ring cavity arrangement, yielding the desired 532 nm light. The filter is able to block residual emissions at 1064 nm and 808 nm and transmit only the signal at 532 nm.

An imaging system (lenses L1 and L2) is used to decrease the laser's spot size. The nonlinear crystal is located at the position where the beam waist of the pump beam is $w_0 = 100$ μm. The nonlinear crystal for these experiments is a $L = 1$ mm long periodically-poled lithium niobate (PPLN) crystal (Covesion). It is pumped by the $\lambda_p = 532$ nm photons, and by means of spontaneous parametric down-conversion (SPDC), two lower-frequency photons, signal and idler, are generated with central wavelengths of 1550 nm and 810 nm, respectively.

A half-wave plate (HWP) before the crystal is used to align the polarization of the pump beam for achieving type 0 phase matching. In this way, we also profit from using the highest nonlinear coefficient of the nonlinear crystal. The pump, signal, and idler photons all have different frequencies, but they have the same vertical polarization. This type of configuration, as described in Chapter 2, is known as non-degenerate, collinear, type-0 parametric down-conversion.

The spectrum of down-converted photons varies as a function of the temperature, resulting in various phase-matching conditions for each of the temperatures (see Appendix7 for more details). To control the temperature, the nonlinear crystal is mounted inside an oven (PV20 from Covesion). The oven is coupled to a temperature controller (OC2 from Covesion) that allows for temperature adjustments with a precision of 0.01 C and a maximum working temperature of 200 C. We found that the temperature at which the SPDC spectrum is centered at the desired wavelengths is 126.5 ºC.

A long-pass filter (IF2) is located after the nonlinear crystal to block the pump wavelength. The signal and idler photons are separated by a short-pass dichroic mirror (DM) and coupled into single-mode fibers (SMF) using an aspheric lens of focal length of $f = 11$ mm for each of them.

The Coincidence detection system

Coincidences between signal (1550 nm) and idler (810 nm) photons can be measured using different techniques. Here we use one of the most frequently used systems, known as *Start-Stop*. When an idler photon arrives at the idler photon counting module detector, a TTL pulse is generated. This pulse is sent to the signal photon counting module detector where it triggers the *start* of the clock of this second detector. The arrival time of the TTL pulse determines the moment at which the second detector starts to count photons. If a signal photon arrives at the second detector before the end of the detection window (2.5 ns), a coincidence is counted. When a photon arrives outside the detection window, no coincidence is counted. When the detection window ends or a coincidence is detected, the clock *stops*, and the process starts again. In this Project, the idler single-photon detector (D1, Perkin-Elmer SPCM-AQRH) is used as a trigger to activate the signal single-photon detector (D2, Id Quantique 201), with a detection window of 2.5 ns. An FPGA (Abacus, Tausand, AB1004) is used to monitor the counts of each detector. Single-mode fibers are used to increase the optical path of signal photons and thus delay them. Typical values of optical delays are around 60 ns. The single photon detector *Id Quantique* can introduce an additional electronic delay of the start of the coincidence window, with values between 0 and 25 ns with increments of 0.01 ns.

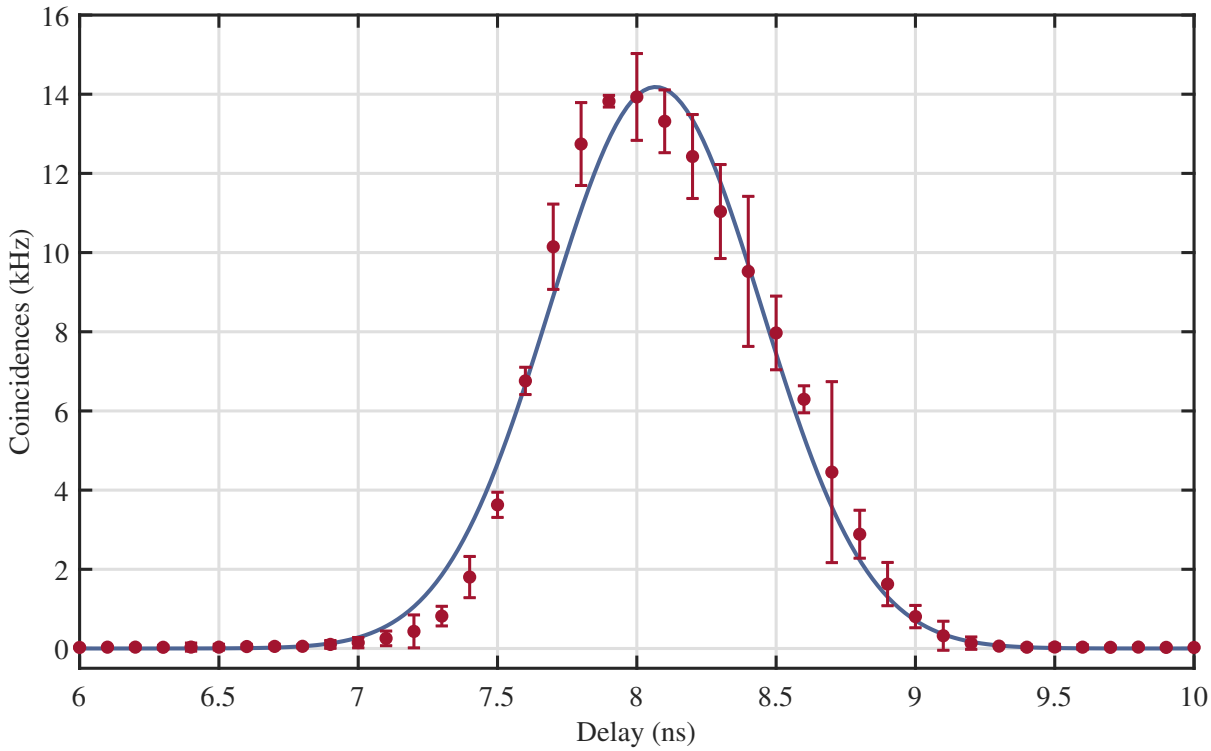

Figure. 3 Flux rate of signal/idler coincidences (coincidences/s) as a function of the time delay set between signal and idler photons. The red points correspond to the experimental results and the solid line is a Gaussian fit with fidelity $R^2 = 0.99$. The Gaussian fit has a FWHM width of 1 ns.

This detection system implies that the signal photons must arrive at D_2 after the idler photons arrive at D_1. Moreover, the delay between them must be smaller than the duration of the coincidence window. The time delay between the signal and idler photons must be carefully set and controlled. This can be done in two ways, first, by increasing the optical path of one of the photons (using mirrors or optical fibers) so that the photons arrive later at the detector, or, by electronically delaying the start of the coincidence window.

Figure 3 shows the number of coincidences/s as a function of the time delay between signal and idler photons. A Gaussian fit (solid line) was used to estimate the full-width half maximum (FWHM) of this curve, which is 1 ns. The experimental data showed that when using a pump power of $\sim$ 30 mW, the maximum number of coincidences (14×10^3 coincidences/s) is obtained at a delay of 8 ns. The coincidences outside the detection window correspond to the accidental coincidences, approximately 20 coincidences/s. These numbers are used as a reference for setting the correct delays in the measurements.

Two types of experiments

We will do two kinds of experiments:

- **Profiting from advanced technology at the Telecomm window for making extremely narrowband frequency filters at the idler (810 nm) frequency band**. The first measurement uses the setup shown in Fig. 2 without the monochromator. Here we aim at demonstrating the use of advanced technology concerning frequency filters at the Telecomm frequency band to analyze filters at the idler frequency band (810 nm). The filter (F) to be analyzed (LL01-810-12.5, Semrock) has a central wavelength at 810 nm (inside the idler frequency band) and a bandwidth between 3.1 and 5.1 nm (as given by the manufacturer). After passing through the filter the idler photons are coupled into single-mode fibers (SMF) and directed to the single-photon detector D1. This detector is a single photon counting module (Perkin Elmer, SPCM-AQRH) with a detection efficiency of approximately 55 %.

  The signal photons are coupled into a SMF and directed to the programmable optical filter (Waveshaper 1000s, Finisar). With the programmable filter, filters with arbitrary shapes can be designed from 1535 to 1562 nm with a minimum bandwidth of 0.08 *nm* (see Appendix 8 for more tails on the principle of operation of the programmable filter). In this case, a square filter with a bandwidth of 0.5 nm was used. The central frequency of the filter was tunned from 1535 to 1562 nm in steps of 0.125 nm. At each point, the number of coincidences between signal and idler photons were counted. After the filter, the signal photons are sent to the single-photon detector D2, a single photon counting module (Id quantique 201) with a maximum detection efficiency of $\sim$ 25%. An FPGA (Abacus, Tausand, AB1004) is used to monitor the counts of each detector.

- **Analyzing frequency filters with complex spectral shapes at the Telecomm window**. The goal of the second part of the experiment is to demonstrate the feasibility of analyzing filters with complex spectral shapes at the signal frequency band, i.e. 1550 nm. The second measurement uses the setup shown in Fig. 2 without the filter (F) analyzed in the previous experiment. The signal photons are coupled into a SMF, connected to the programmable filter, and detected by the single photon counting module *Id quantique*. The spectrum is measured by means of coincidences using a monochromator (microHr, Horiba) that works at the idler frequency band. The monochromator has one entrance and one exit slit and a diffraction grating that is coupled to a motorized rotation stage. By rotating the grating, a spectral scan can be performed between 200 and 1100 nm with steps of 0.05 nm. In this case, the monochromator is programmed to perform a scan from 802 to 820 nm in steps of 0.1 nm. At each point, the singles and coincidences are recorded. After the monochromator, the photons are coupled into a multimode fiber (MMF) and detected by the single photon counting module (Perkin Elmer, SPCM-AQRH).

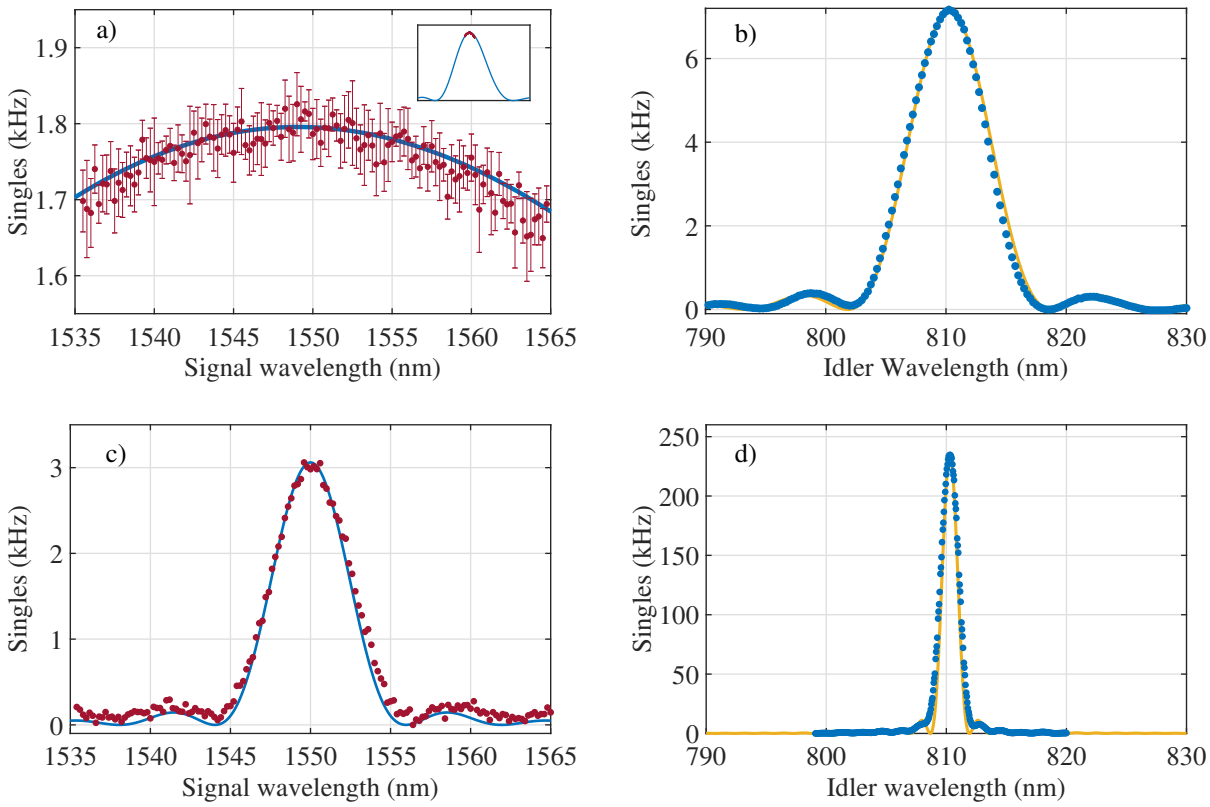

Figure. 4 Spectrum of the down-converted photons. Experimental results (dots in blue and red) and theoretical calculations (solid lines) of the singles spectrum obtained using a PPLN crystal with different lengths: (a) and (b): $L = 1\ mm$; (c) and (d) $L = 5\ mm$.

3.3 Experimental Results

Measurement of the SPDC spectrum

The SPDC spectrum was measured without any filters to obtain the bandwidth of down-conversion. This measurement was repeated for different temperatures until the signal and idler spectrum were centered at the desired central signal and idler wavelength. Fig. 4 shows the experimental results for a PPLN nonlinear crystal of length $L = 1mm$ (a,b) and $L = 5$ mm (c,d). The single photon count rate of the signal photons (a, c) is provided by the *Id quantique* single-photon counting module and shows the spectrum as the programmable filter is tuned. As described previously, a square pulse with a bandwidth of 1 nm and a central frequency varying from 1530 to 1565 nm is uploaded to the programmable filter. The single photon count rate of the idler photons (b, d) is provided by the *Perkin-Elmer* single-photon counting module and shows the spectrum as the monochromator is tuned from 790 to 830 nm.

The solid lines in Fig. 4 correspond to the singles spectrum described in Eq. 24, evaluated for each crystal length and using the Sellmeier equations described in Appendix 7. The match between the experimental data (dots) and the theory (solid lines) can be clearly observed,

Crystal length	***Theoretical calculations***		***Experimental results***	
	$\Delta\lambda_{1550}$ (nm)	$\Delta\lambda_{810}$ (nm)	$\Delta\lambda_{1550}$ (nm)	$\Delta\lambda_{810}$ (nm)
1 mm	27.23	7.40	-	7.24
5 mm	5.45	1.44	5.40	1.71

Figure. 1 Bandwidth at FWHM of the SPDC spectrum for PPLN crystals with different lengths. The bandwidth for the spectrum at 1550 nm for L=1nm is not reported since the scanning range is smaller than the bandwidth of the spectrum.

especially in Fig. (b) and (c), which show the characteristic lobes of the sinc function. The bandwidth (at FWHM) of the down-converted photons was measured for both the theoretical and the experimental results. These are summarized in Table1. The spectral bandwidth of the signal photons generated with the 1 mm PPLN [shown in Fig.4 (a)] is around 60 nm at $1/e^2$ width. Since the programmable filter has an operating frequency range from 1528 to 1567 nm, only the top part of the spectrum is measured. This is why the bandwidth at FWHM of this spectrum was not measured.

The spectral bandwidth of the down-converted photons determines the spectral range that can be used to measure the absorption spectrum of a sample. As mentioned before, the filter to be analyzed at 810nm has a bandwidth between 3.1 and 5 nm. Therefore, the bandwidth of the 5 *mm* PPLN is too narrow to scan the complete shape of the filter. The 1 mm PPLN has a broader spectrum, and at 1550nm its shape is almost flat [see Fig. 4 (a)]. This explains why the 1 mm PPLN was chosen to do these measurements.

One disadvantage of using the 1 mm crystal, compared to using the 5 mm, is its conversion efficiency. The efficiency that can be achieved with a PPLN crystal depends mainly on the pump power and the length of the nonlinear crystal. The longer the crystal, the greater the conversion efficiency. This can be seen in the number of singles/s shown in Fig. 4. The maximum number of singles/s for the idler photons is 1.8kHz and 3kHz for the 1mm and 5mm crystals, respectively.

Measurement of the spectral shape of a filter centered at 810nm

The main purpose of this experiment is to show, in a *proof of concept* experiment, that by measuring the coincidences between signal and idler photons one can use the technology available at the signal frequency to measure the absorption spectrum of an object at the idler frequency. To do this, a spectral filter (LL01-810-12.5, Semrock) with central wavelength at 810 nm and bandwidth of $\approx$ 3.1 nm was measured. This is a low-cost, commercially available spectral filter with one of the shortest bandwidths (at 810 nm) that we have found. The spectral scan was performed by a square pulse with a bandwidth of 0.5 nm, designed using the programmable filter. The filter is tuned from 1535 to 1565 nm, and at each point, the coincidences between signal and idler photons were measured following the scheme and

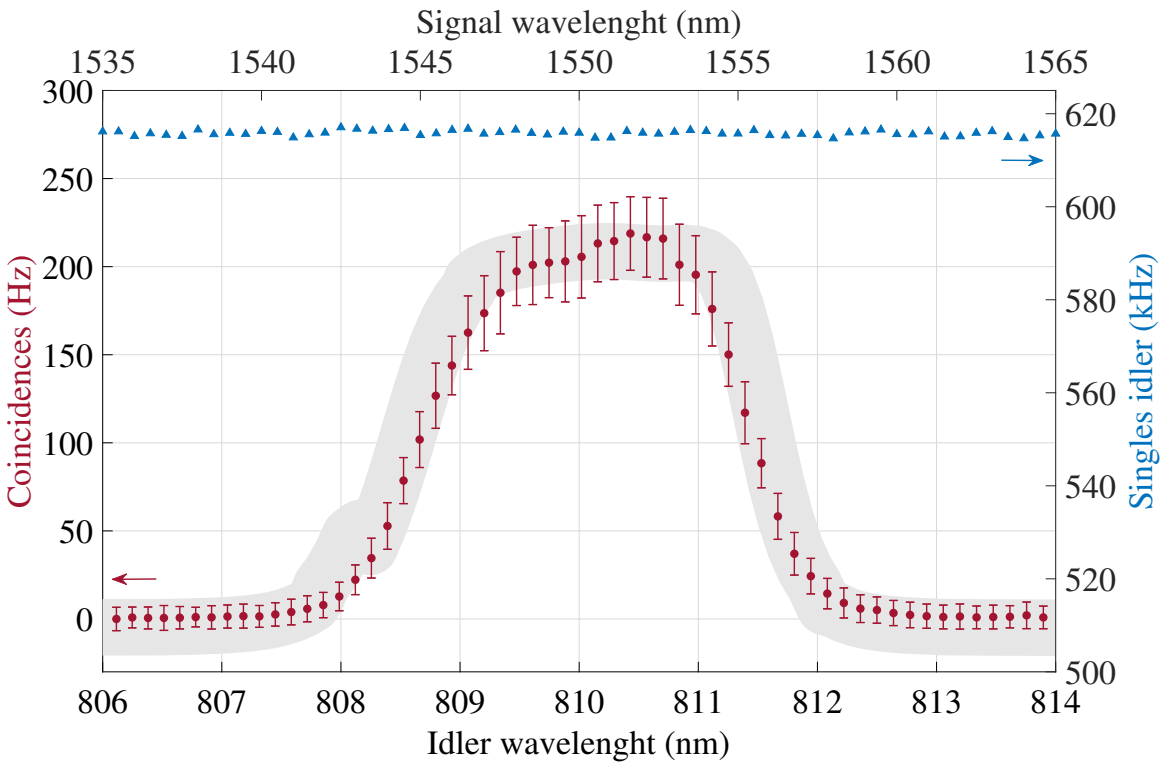

Figure. 5 Measurement of a filter with central frequency at 810 nm. The red points are the measured coincidences per second, that correspond to the spectrum of the filter analyzed. A width (FWHM) of 2.73 nm was measured using this data. The blue triangles are the idler photons measured (singles). The solid gray line represents the uncertainty of the spectral shape provided by the manufacturer.

constraints explained in the previous subsection.

The experimental settings values used for this experiment are:

- Pump beam power: $P = 40$ mW.
- Coincidence detection window: $T_d = 2.5$ ns.
- Total detection window (sampling time): $T_0 = 1s$.
- Idler (trigger) rate: 616×10^3 counts/s.

The experimental results are shown in Fig. 5. The coincidences between signal and idler photons (red circles) clearly show the shape of the analyzed filter. The solid gray line represents the uncertainty of the spectral shape provided by the manufacturer. Since the spectral scan is performed with the programmable filter, the coincidences are measured as a function of the signal wavelength band, centered at 1550 nm. To recover the shape of the filter at the idler wavelength band, centered at 810 nm, we use the energy conservation relation: $1/\lambda_p = 1/\lambda_s + 1/\lambda_i$. By making this change, we calculated the bandwidth (FWHM) of the filter to be 2.37 nm. The singles for the idler photons correspond to the blue triangles.

The resolution of this system is determined by the bandwidth of the filter uploaded to the programmable filter, $\Delta\lambda_s = 0.5nm$. Using Eq. 1, the resolution at the idler wavelength is $\Delta\lambda_i = 0.1365\,nm$. This is at least one order of magnitude better than the bandwidth of commercially available spectral filters at 810 . For instance, the filter analyzed in this section has one of the shortest bandwidths. Filters with a narrower bandwidth, as short as 0.08 nm, can be designed using the programmable filter. Nevertheless, narrowing the filter decreases the singles flux rate at the signal frequency, and therefore the number of coincidences/s. This reduction can be overcome by increasing the data acquisition time.

Measurement of a frequency filter with complex spectral shapes at the Telecomm window

For this second part of the experiments, we want to demonstrate that we are able to unveil complex spectral shapes as well. We take advantage of the programmable filter to generate filters with arbitrary shapes around 1550 nm and will recover its shape using a tunable monochromator at 810 nm. The experimental settings used for this experiment are:

- Pump beam power: P = 1.5 W.
- Coincidence window: T_d = 2.5 ns.
- Total detection window (sampling time): $T_0 = 30s$,

The left column of Fig. 6 shows the filters uploaded to the programmable filter. The right column corresponds to the coincidences measured as the monochromator is tuned from 802 to 820 nm. Here we have used the relationship

$$\frac{1}{\lambda_p} = \frac{1}{\lambda_s} + \frac{1}{\lambda_i} \tag{40}$$

to find the equivalent wavelength at the signal frequency.

It can be seen, from the right column of Fig. 6, a clear match between the experimental data (blue dots) and the theory (solid line), described at the beginning of Chapter 3. The position of the peaks in the coincidences spectra matches the position of the peaks in the filter under study. Nevertheless, there is a difference in the width of the peaks [see for instance Fig. 6 (a) and (f)]. This is because the coincidences spectrum is the result not only of the shape of the filter under study but is its convolution with the spectral shape of the monochromator. The bandwidth of the monochromator is 1 nm (see measurement in Appendix 9) following the same methodology described in the previous section, i.e. the monochromator was centered at 810 nm, and the programmable filter was tuned from 1535 to 1565 nm. This result was used for the theoretical calculations.

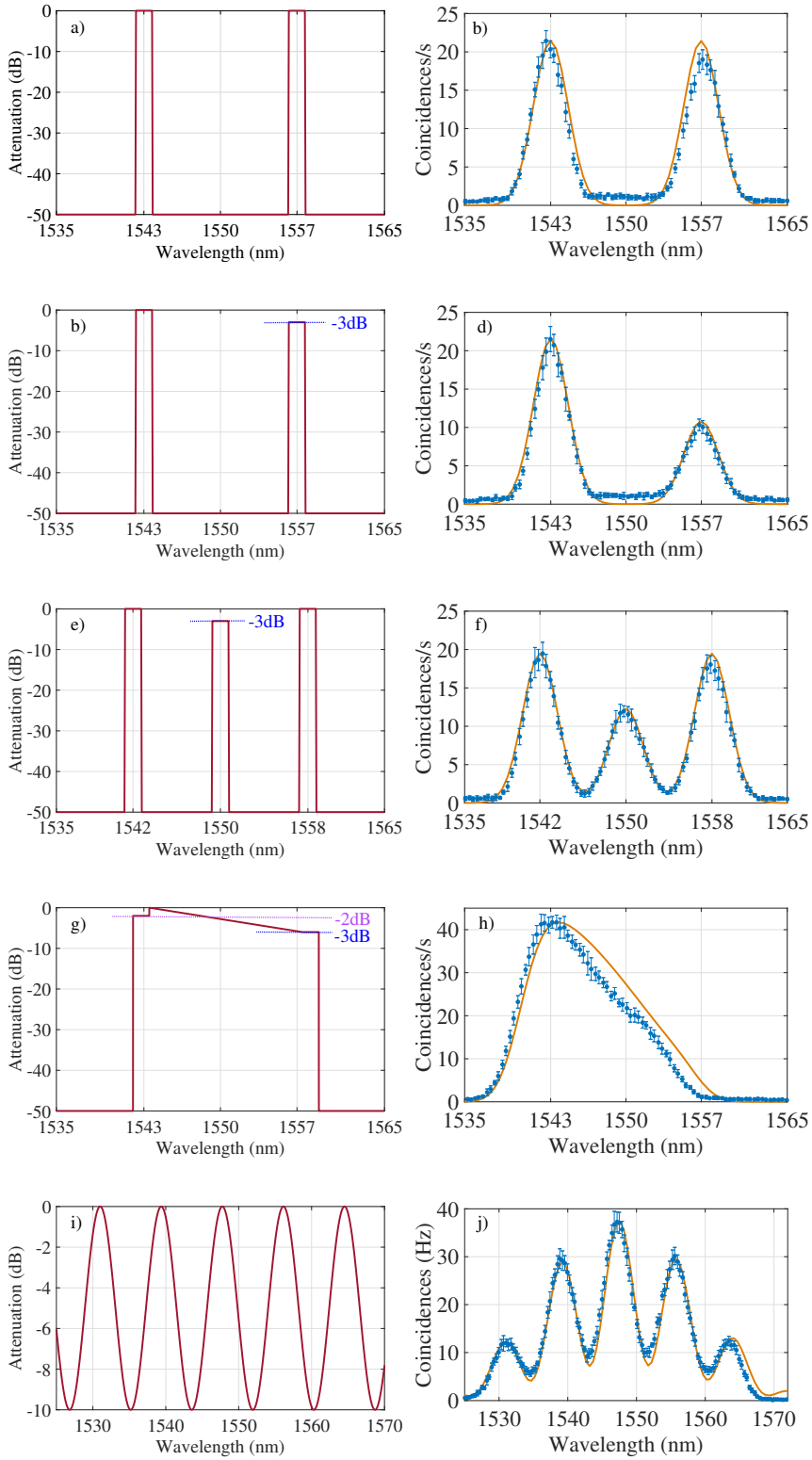

Figure. 6 Measurement of filters with arbitrary shapes at the signal frequency. The left column corresponds the filter uploaded to the programmable filter. The right column shows the coincidences/s as a function of wavelength, measured with a monochromator. The blue dots correspond to the experimental data, and the orange solid line is the theory.

Figures 6 (b) and (c) are good examples of how the differential attenuation of a filter can be successfully detected using this technique. The peaks in the input filters have an attenuation of 0dB (100% transmission), and -3dB (%50 transmission). The coincidences measured corresponding to each peak are 20, and 10 coincidences/s for the 100% and 50% transmission, respectively. This shows that it is possible to detect differential absorption, peaks with different amplitudes, accurately.

An interesting case that shows the importance of having a *flat top* SPDC spectrum is shown in Fig. 6 (i) and (j). Here a sinusoidal filter was uploaded to the programmable filter. The recovered filter shows correctly the number of oscillations and their position, nevertheless, the number of coincidences/s is different for each peak. This effect is due to the bandwidth of the SPDC spectrum shown in Fig. 4 (a). The result shown in Fig. 6 (j) is the SPDC spectrum multiplied by the filter, which gives this modulation effect to the experimental result.

3.4 Limitations of the method

We have shown and demonstrated that the use of quantum correlations between photons at different frequencies allows to use better technology that might exist at one frequency band, for making more accurate measurements at another frequency band where worse technology exists. For instance, we have seen that the existence of commercially available narrowband filters with extremely narrow bandwidths at the Telecomm frequency band allows measuring spectra at the frequency band around 810 nm with a high-frequency resolution, even though low-cost and commercially available filters with such narrow bandwidth do not exist at this frequency band.

However, the method demonstrated shows three main drawbacks. The first one is that one still needs to measure at the two frequency bands: signal and idler frequency bands. Therefore one needs efficient detectors at both frequency bands. We have seen that, even though we can avoid using filters at the frequency band around 810, we still need to detect photons at this frequency band. At certain frequency bands, there might not be efficient detectors.

The second drawback is that one needs to measure coincidences between signal and idler photons. The measurement of coincidences always introduces a certain level of difficulty to experimental setups. There is no information about a spectral shape in a frequency band measuring single detections at the other frequency band.

The third drawback is that in the low parametric gain regime, photon fluxes generated and detected are small, which requires long integration times. One possible escape to this situation would be to take this method to the high parametric gain regime ($G \gg 1$) where higher photon fluxes can be generated. However, this is not a feasible option. The method works

because of the unique quantum correlations existing between a pair of signal and idler photons. But increasing the gain increases the probability to detect a signal/idler coincidence between photons not belonging to the same pair. These coincidence counts do not bear any information about frequency filters in different frequency bands.

Following the theoretical analysis of Section 3.1, we can see that the coincidences between signal/idler photons not belonging to the same pair scales with the gain G as $\sinh^4 G$, while coincidences between signal/idler photons belonging to the same pair go as $\sinh^2 G$. In the low parametric gain regime ($G \ll 1$), we have low photon fluxes, but coincidences of photons belonging to the same pair dominate, i.e., $\sinh^2 G \gg \sinh^4 G \longrightarrow G^2 \gg G^4$. In the high parametric gain regime ($G \gg 1$), we have higher photon fluxes, however, coincidences of photons not belonging to the same pair now dominate, i.e., $\sinh^4 G \gg \sinh^2 G$, hiding information about spectral shapes in different frequency bands.

4 Quantum spectroscopy with a SU(1,1) interferometer

The well-known Mach-Zehnder interferometer contains two beam splitters, one at the input and another one at the output of the interferometer. We will show in this chapter that the drawbacks described in Section 3.4 can be overcome using Mach-Zehnder type interferometers that contain inside second-order nonlinear crystals, that substitute the beam splitters of *standard* Mach-Zehnder interferometers. Sometimes these interferometers are referred to as *nonlinear interferometers* [36]. One word of caution: although this term is nowadays used often, it can create some confusion since a Mach-Zehnder interferometer where optical beams see a refractive index proportional to the intensity (nonlinear optical Kerr effect) is also referred to as nonlinear interferometers [37].

The original idea of this kind of interferometer comes from the demonstration in 1991 of the concept of *induced coherence without induced emission* by the group of Leonard Mandel at Rochester University [13, 14]. Fig. 7 shows a simplified sketch of the interferometer, which we can refer to as *Mandel-type* interferometer. Notice that only the idler beam generated in the first parametric down-conversion crystal (NLC_1) passes through the second nonlinear crystal (NLC_2). Although this is not the type of interferometer that we will consider here, most of the things that we will derive below would also apply to a Mandel-type nonlinear interferometer. Mandel-type interferometers have been considered recently for many applications [12, 17, 38].

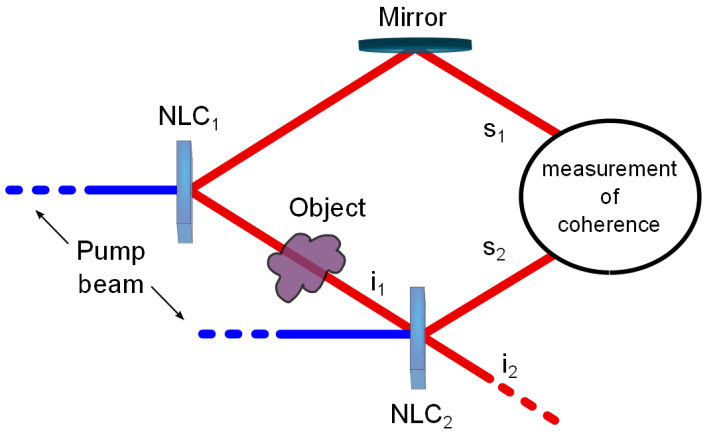

Figure. 7 Simplified sketch of an interferometer based on the concept of induced coherence. $NLC_{1,2}$ are nonlinear crystals; s, i refer to the signal and idler photons, with sub-indexes indicating from which crystal they are emitted. Image taken from Valles et al., Phys. Rev. A **97**, 023824 (2018).

A SU(1,1) interferometer

We will consider a SU(1,1) interferometer [see Appendix 10 for an explanation of the origin of the term SU(1,1)] for naming the interferometer). This type of interferometer was first proposed by Yurke et al. [15] in 1986 with the aim of increasing the sensitivity of phase estimation. We can refer to this interferometer as *Yurke-type* interferometer to differentiate it from the Mandel-type interferometer. The main difference between both types of interferometers is that in a SU(1,1) interferometer, both signal and idler photons generated from the first nonlinear crystal are injected into the second crystal, while in a Mandel-type interferometer, only idler photons are injected in the second nonlinear crystal.

Figure 8 shows a particular configuration of a SU(1,1) interferometer using a single nonlinear crystal (NLC). This configuration is very convenient for its experimental implementation since it makes use of a single nonlinear crystal [17]. The pump beam illuminates the NLC where the signal (s_1) and idler (i_1) waves are generated. The pump and the signal are transmitted through a dichroic mirror, while the idler is reflected. The pump and the signal are reflected by a mirror and enter again the nonlinear crystal. The distance traveled by the signal beam before reaching the crystal is z_s. We consider a reflectivity rs that accounts for frequency-independent losses in the signal path due to the optical elements. The idler beam interacts with a lossy object with reflectivity $r_i(\Omega)$ and is reflected back onto the crystal, traveling a total distance z_i. The pump beam illuminates the same nonlinear crystal backwards, and the signal (s_1) and idler (i_1) are also injected back into the nonlinear crystal. Signal (s_2) and idler (i_2) waves are generated after the second pass by the nonlinear crystal. Finally, the spectrum and/or the flux rate of the signal photons s_2 is the quantity measured by detector D.

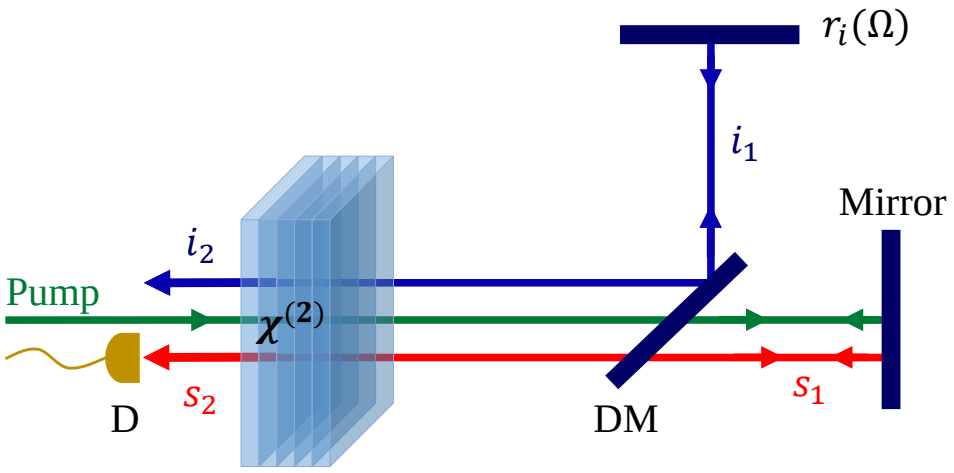

Figure. 8 Scheme of a SU(1,1) interferometer [17].

4.1 Quantum derivation of the shape of the spectrum of signal photons s_2 measured.

The spectrum of signal photons measured at the output of the second nonlinear crystal, under the plane-wave approximation, is [17]

$$S(\Omega) = |V_{s_2}(\Omega)|^2 \left[1 - |H_i(-\Omega)|^2\right] \tag{41}$$
$$+ \left|U_{s_2}(\Omega)V_{s_1}(\Omega)H_s(\Omega)\ \exp[i\varphi_s(\Omega)] + U_{i_1}^*(-\Omega)V_{s_2}(\Omega)\ H_i^*(-\Omega)\exp[-i\varphi_i(-\Omega)]\right|^2 .$$

The functions U_{s_2}, U_{i_1}, V_{s_1} and V_{s_2} are given by Eq. (4). U_{i_1} and V_{s_1} refer to the first pass by the nonlinear crystal, where Spontaneous Parametric Down-Conversion (SPDC) takes place, while U_{s_2} and V_{s_2} refer to the second pass by the nonlinear crystal, where Optical Parametric Amplification (OPA) takes place. We assume that $|H_s(\Omega_S)| = r_s$ is constant and describes only some frequency-independent losses in the signal path.

Making use of the relationships

$$U_{s_2}(\Omega)U_{i_1}(-\Omega) = |U_s(\Omega)|\,|U_i(-\Omega)|,$$
$$V_{s_1}(\Omega)V_{s_2}^*(\Omega) = |V_{s_1}(\Omega)|\,|V_{s_2}(\Omega)|\ \exp(i\varphi_p), \tag{42}$$

where $\varphi_p = \varphi_{p_1} - i\varphi_{p_2}$ is the phase difference between the pump beams that illuminate the nonlinear crystal in the first and second pass by the nonlinear crystal, we obtain that

$$S(\Omega) = |V_{s_2}(\Omega)|^2 \left[1 - |H_i(-\Omega)|^2\right] + r_s^2 |U_{s_2}(\Omega)|^2 |V_{s_1}(\Omega)|^2 \tag{43}$$
$$+|U_{s_1}(-\Omega)|^2 |V_{s_2}(\Omega)|^2 |H_i(-\Omega)|^2 + 2r_s |U_{s_2}(\Omega)||U_{i_1}(-\Omega)||V_{s_1}(\Omega)||V_{s_2}(\Omega)||H_i(-\Omega)| \cos\varphi.$$

The phase φ is

$$\varphi = \frac{\omega_s z_s + \omega_i z_i}{c} + \frac{\Omega}{c}\Delta z + \varphi_p + \delta(\Omega), \tag{44}$$

where $\Delta z = z_s - z_i$ is the path length difference between signal and idler photons before passing by the nonlinear crystal for the second time. $\delta(\Omega)$ is the phase introduced by the filter in the idler path. For the sake of simplicity, we assume that $\delta(\Omega)$ is constant and focus our attention on how measuring the spectral shape of the filter.

In the two passes by the nonlinear crystal, the pump beam can have a different energy, so the gains of parametric down-conversion for each pass can be different, G_1 and G_2. The functions V_{s_1} and V_{s_2} can thus be approximated as

$$|V_{s_1}(\Omega)|^2 = \sinh^2 G_1 \ \exp\left(-\pi\frac{\Omega^2}{B^2}\right),$$
$$|V_{s_2}(\Omega)|^2 = \sinh^2 G_2 \ \exp\left(-\pi\frac{\Omega^2}{B^2}\right), \tag{45}$$

where B is the bandwidth of parametric down-conversion. B is much bigger than the bandwidth of the filter H_i.

We can write

$$S(\Omega) = \left\{\sinh^2 G_2 + r_s^2 \sinh^2 G_1\right\} \ \exp\left(-\pi\frac{\Omega^2}{B^2}\right)$$
$$+\sinh^2 G_1 \ \sinh^2 G_2 \left[r_s^2 + |H_i(-\Omega)|^2\right] \ \exp\left(-2\pi\frac{\Omega^2}{B^2}\right) \tag{46}$$
$$+2r_s \ \sinh^2 G_1 \ \sinh^2 G_2 \, |H_i(-\Omega)| \cos\varphi \exp\left(-\pi\frac{\Omega^2}{B^2}\right)$$
$$\times\sqrt{1 + \sinh^2 G_1 \ \exp\left(-\pi\frac{\Omega^2}{B^2}\right)}\sqrt{1 + \sinh^2 G_2 \ \exp\left(-\pi\frac{\Omega^2}{B^2}\right)}.$$

For obtaining Eq. (46) we have made use of the relationship $|U_s(\Omega)|^2 - |V_s(\Omega)|^2 = 1$. For the case of interest here, with $G_1 = G_2 \equiv G$, we have

$$S(\Omega) = \sinh^2 G\Big\{1 + r_s^2 + 2r_s\,|H_i(-\Omega)|\cos\varphi\Big\}\,\exp\Big(-\pi\frac{\Omega^2}{B^2}\Big)$$
$$+\sinh^4 G\,\Big\{r_s^2 + |H_i(-\Omega)|^2 + 2r_s\,|H_i(-\Omega)|\cos\varphi\Big\}\,\exp\Big(-2\pi\frac{\Omega^2}{B^2}\Big). \tag{47}$$

Equation (47) is the main result of this section.

4.2 How to retrieve the spectral shape of the frequency filter $H_i(\Omega)$

First method

The most straightforward way is to use at the detection stage, a narrowband filter with bandwidth B_d centered at frequency Ω_0 before detecting the signal photons. In the low parametric gain ($G \ll 1$), the flux rate $R_s(\Omega_0) = S(\Omega_0)B_d$ (photons/s) of signal photons detected is

$$R(\Omega_0) = B_d\,G^2\,\Big\{1 + r_s^2 + 2r_s\,|H_i(-\Omega_0)|\cos\varphi\Big\}\,\exp\Big[-\pi\frac{\Omega_0^2}{B^2}\Big], \tag{48}$$

where we use the approximation $\sinh^2 G \sim G^2$. For the sake of simplicity, we consider $\varphi = 0$.

To get rid of the effect of the spectrum of PDC and isolate the sought-after spectrum of the filter $H_i(-\Omega)$, we subtract from Eq. (48) the signal spectrum that we would obtain by blocking the idler beam i_1, i.e., $R_0(\Omega) = B_d\,G^2\,\{1 + r_s^2\}\exp[-\pi\Omega_0^2/B^2]$, so we can write

$$R(\Omega_0) - R_0(\Omega_0) = 2r_sB_d\,G^2\,|H_i(-\Omega_0)|\,\exp\Big[-\pi\frac{\Omega_0^2}{B^2}\Big]. \tag{49}$$

Since the spectrum of the filter is much smaller than the spectrum of PDC, the effect of the term $\exp[-\pi\Omega_0^2/B^2]$ should be small, as we will see with an example in Section 4.3.

In the high parametric gain regime ($G \gg 1$), we have

$$R(\Omega_0) = B_d\,\sinh^4 G\,\Big\{r_s^2 + |H_i(-\Omega_0)|^2 + 2r_s\,|H_i(-\Omega_0)|\cos\varphi\Big\}\,\exp\Big[-2\pi\frac{\Omega_0^2}{B^2}\Big]. \tag{50}$$

Using the same procedure explained above, we obtain

$$R(\Omega_0) - R_0(\Omega) = B_d\,\sinh^4 G\,\Big\{|H_i(-\Omega_0)|^2 + 2r_s\,|H_i(-\Omega_0)|\Big\}\,\exp\Big[-2\pi\frac{\Omega_0^2}{B^2}\Big]. \tag{51}$$

Second method

In Eq. (46) there are terms that depend on the value of the phase, φ, and terms that do not. If we measure the flux rates $R(\Omega)$ for two different values of the phase, φ_1 and φ_2, and subtract the results obtained, $R_1(\Omega)$ and $R_2(\Omega)$, we obtain that

$$\begin{aligned}\Delta R(\Omega) &= R_1(\Omega) - R_2(\Omega) \\ &= 2r_s\, B_d\, |H_i(-\Omega)| \Big[\cos\varphi_1 - \cos\varphi_2 \Big] \Big\{ \sinh^2 G\, \exp\Big(-\pi \frac{\Omega^2}{B^2} \Big) + \sinh^4 G\, \exp\Big(-2\pi \frac{\Omega^2}{B^2} \Big) \Big\}.\end{aligned} \tag{52}$$

Inspection of Eq. (44) shows that we can change the value of φ by modifying the path length difference Δz between signal and idler photons, or the pump beam phase difference φ_p, with the help of piezoelectric actuators. If we take into account that the bandwidth of PDC is much bigger than the bandwidth of the filter, we have that

$$|H_i(-\Omega)|^2 = \frac{|\Delta R(\Omega)|}{2\, r_s\, B_d\, \sinh^2 G\, (1 + \sinh^2 G) \Big| \cos\varphi_1 - \cos\varphi_2 \Big|}. \tag{53}$$

Importantly, we notice that we can measure the spectral shape of the filter in the high parametric regime, where there are higher photon fluxes. This allows to use less sensitive detectors and reduce the detection time required to obtain high-quality measurements with a high signal-to-noise ratio.

Third method

The second method requires knowledge of the values of the phases φ_1 and φ_2. An alternative method that does not require setting the phase φ to specific values consist on measuring the flux rates $R(\Omega)$ for multiple phases and measuring the resulting visibility for each frequency Ω

$$\mathrm{V} = \frac{R^{max}(\Omega) - R^{min}(\Omega)}{R^{max}(\Omega) + R^{min}(\Omega)} \tag{54}$$

Making use of Eq. (47), we obtain that the visibility is

$$\mathrm{V} = |H_i(-\Omega)|\, \frac{2r_s \sinh^2 G(1 + \sinh^2 G)}{(1 + r_s^2)\, \sinh^2 G + (r_s^2 + |H_i(-\Omega)|^2)\, \sinh^4 G} \tag{55}$$

In the low parametric gain regime ($G \ll 1$) we obtain [39]

$$\mathrm{V} = |H_i(-\Omega)|\, \frac{2r_s}{1 + r_s^2} \tag{56}$$

while in the high parametric gain regime ($G \gg 1$), the visibility is [17]

$$\mathrm{V} = \frac{2r_s\,|H_i(-\Omega)|}{r_s^2 + |H_i(-\Omega)|^2} \tag{57}$$

4.3 First method: An example

As an example, we consider two filters at the Telecomm window (around 1550 nm) with different shapes, as shown in Fig.9 (a) and (b). In an experimental scenario, these filters would be uploaded to the programmable filter and used to filter the signal photons at 1550 nm. We retrieve their spectral shapes by measuring the spectrum of idler photons at 810 nm, using the first method described above. One word of caution: the roles of the signal/idler photons have been reversed in this example. The filter is in the signal path, and we detect idler photons only.

For the sake of simplicity, we assume $r_s = 1$ and $\varphi = 0$. The filter detection bandwidth is $B_d = 2.87$ THz, which corresponds to 1 nm at 810 nm. We consider the low parametric gain with $G = 1 \times 10^{-4}$. The results for the two filters are shown in Fig.9 (c) and (f). To go from the measured idler frequencies to the signal frequencies, we make use of Eq. (40).

Comparing Figs.9 (a) and (g) we observe a very good agreement between the spectral shape retrieved and the target spectral shape. Notice that the spectral shape retrieved in Fig.9 (h) shows a slightly different slope than the target spectrum shown in Fig.9 (b). This is due to the effect of the spectrum of the pump beam as shown in Eq. (49). Its bandwidth is much bigger than the bandwidth of the filter, this is why the effect is so small. However, its presence can not be completely neglected. To mitigate this effect, we would need to use a nonlinear crystal with a larger bandwidth, for instance using a shorter crystal.

For the case with $G = 1 \times 10^{-4}$, the maximum flux rate is 1.15×10^5 photons/s. If we would consider the high parametric gain regime with gain $G = 2$, we would measure a maximum flux rate of 5.3×10^{12} photons/s, which is 7 orders of magnitude bigger than in the low parametric gain regime case. One can achieve even greater values of the parametric gain G [40, 41].

These results show that nonlinear interferometers are a feasible option to do absorption spectroscopy. The main advantage of this method, as previously stated, is that the measurements are done in the most convenient wavelength for efficient detection. Moreover, this scheme allows us to make measurements in the high parametric gain regime, allowing a greater flux rate of photons, which can enhance the sensitivity of the measurements.

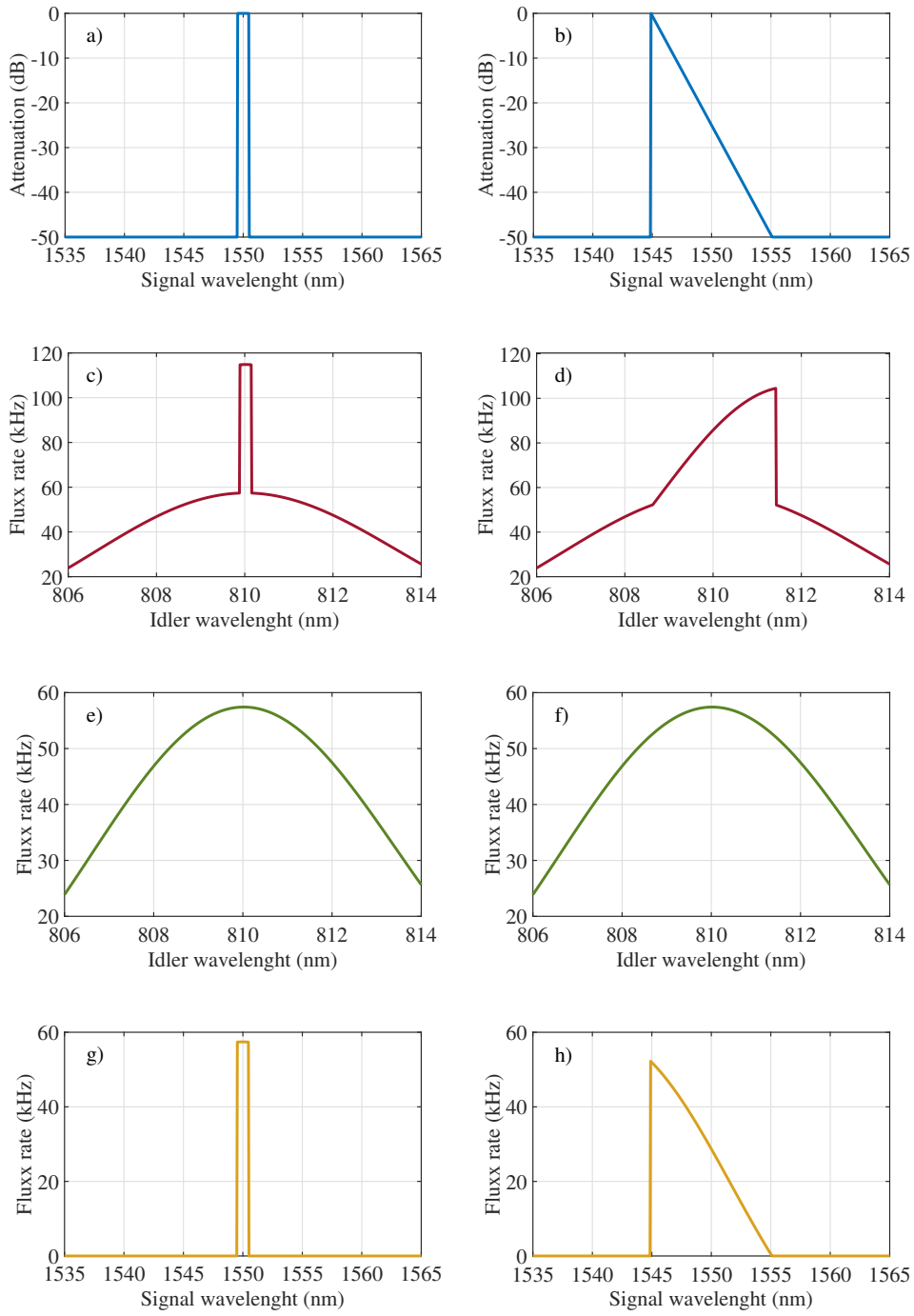

Figure. 9 Example of retrieving the spectral shape of two filters at the signal band (1550 nm) using a SU(1,1) interferometer. We use the first method described in Section 4.2. (a) and (b) (blue): the two filters under study; (c) and (d) (red): Flux rates $R(\Omega)$ of idler photon detected; (e) and (f) (green): Flux rates $R_0(\Omega)$ of idler photons detected without the presence of the filter in the signal path; (g) and (h) (yellow): Result of the subtraction $R(\Omega) - R_0(\Omega)$. Parameters: $G = 1 \times 10^{-4}$ (low parametric gain), $\varphi = 0$, $r_s = 1$, $B_d = 2.87$ THz (1 nm at 810 nm).

5 Discussion and conclusions

In the present work, we have considered two types of absorption spectroscopy configurations based on quantum light. As an example, we have considered how to retrieve the spectral shape of a frequency filter, which is analogous to measuring the absorption spectrum of a sample. The fundamental principles involved are the same. The first scheme makes use of the quantum correlations that exist between signal/idler photons generated in the nonlinear process of spontaneous parametric down-conversion (SPDC). In the experimental configuration that we have implemented in the laboratory (collinear type 0 non-degenerate SPDC), the signal/idler photons generated exhibit naturally a high degree of frequency entanglement [42, 44], although this condition might not be a requisite to do absorption spectroscopy, since frequency correlations without entanglement can also be generated with SPDC in alternative configurations. The second scheme makes use of quantum interference between paired photons generated in two nonlinear crystals. The nature of the interference is determined by the specific spectral shape of the filters, that we can use to retrieve its spectral shape.

The two schemes share some characteristics. They both use $\chi^{(2)}$ nonlinear crystals that do parametric down-conversion (PDC), and in both cases we consider non-degenerate PDC configurations, i.e., signal and idler photons are generated in different frequency bands. Only one photon of the pair (idler photon in our analysis) interacts with the sample. In our experiments, the signal photons are generated in the Telecomm frequency band (around 1550 nm) and the idler photons around 810 nm.

The two schemes show important differences. First, they are based on different physical principles. The first scheme is based on the existence of frequency anti-correlation between signal and idler photons with frequencies $\omega_s + \Omega$ and $\omega_i - \Omega$, respectively. this is due to the use of a quasi-monochromatic pump with a very narrow bandwidth ($\sim$ 5 MHz). The second scheme is based on the principle of quantum interference between two possibilities: signal/idler photons generated in one or the other of two nonlinear crystals. The second difference is that the first scheme requires the measurement of coincidence counts between signal/idler photon pairs, while the second scheme only requires the measurement of signal photons. The third fundamental difference is that the first scheme only works in the low parametric gain regime, while the second scheme works in any parametric gain regime.

Concerning the first scheme, we have done detailed theoretical calculations using the quantum Heisenberg approach, which is a novelty for these kinds of experiments. We have also done several experiments to demonstrate the possibilities of the method. We have used advanced technology for shaping with a narrow bandwidth and an arbitrary spectral shape the spectrum of signal photons, and we have been able to *translate* the advantages of this

technology to another frequency band. Probably this is the first demonstration of this technique of the use of a *real* advanced technology at one frequency band for enhancing a measurement at a different frequency band where an equivalent technology is missing, at least if one considers a commercially available and low-cost option.

In the first set of experiments, we measured the spectral shape of a commercially available filter (LL01-810-12.5, Semrock) at 810 nm with bandwidth $\sim$ 2.7 nm, and obtain experimentally a spectral shape inside the uncertainty given by the manufacturer. This is an *illuminating* example of how using quantum light allowed us to do a measurement that could not do otherwise. We did not have narrowband filters at 810 nm to measure a spectral shape with a bandwidth of $\sim$ 2.7 nm. However, we had a Programmable filter (Waveshaper1000s, Finisar) working at 1550 nm that indirectly could allow *effective* narrowband filtering at 810 nm through quantum correlations and the measurement of coincidences. In a second set of experiments, we demonstrated that we could measure arbitrary spectral shapes, in a way analogous to how we would measure the absorption spectrum of a sample. The Programmable filter at 1550 nm was the *wonderful* device that allowed us to create all types of spectral shapes in a straightforward way.

Concerning the second scheme, we have made detailed theoretical calculations that show the potentiality of the method, and highlight the limitations of the first scheme:

- We do not need to measure coincidence counts, that can be a complicated task, especially when considering photons at different frequencies.
- We only need to detect light at one frequency band, the light that does not interact with the sample, so we can choose the most optimum wavelength for detection.
- We can work on the high-parametric gain regime, where there are higher photon fluxes, and therefore measurements can be made faster with lower sensitivity detectors

We plan to continue this research topic by implementing a SU(1,1) interferometer for absorption spectroscopy and show experimentally the advantages described in this Project. We can do experiments in the low parametric gain regime at ICFO, where we have all the elements required, as shown in this Project and can be seen in [39]. For the high parametric gain regime, one needs to use a pulsed laser (picosecond pulses) that generates high energy pulses so the average power can be up to hundreds of mW. For this we would collaborate with the groups of M. Chekhova at the Max Planck Institute for the Science of Light (Erlangen, Germany), and the group of M. Grafe at Darmstadt University (Darmstadt, Germany). We keep collaborations with both groups as can be seen in [17].

6 Summary of main results of this Project

1. We have demonstrated a *real* example of how to make use of advanced technology at one frequency band (around 1550 nm) to perform high-resolution frequency measurements at another frequency band (around 810). There is no similar commercially available technology at this frequency band. We have considered narrowband filtering with arbitrary spectral shape around 1550 nm using a commercially available Programmable optical filter (Waveshaper 1000s Finisar). This is an example of using quantum correlations for *frequency translation* of technology.

2. We have implemented experimentally a collinear type 0 non-degenerate temperature-controlled Spontaneous Parametric Down-Conversion (SPDC) source to generate frequency-entangled photons. We have also implemented a system to measure coincidence counts between single photons at different frequency bands (810 and 1550 nm). At 810 nm we use a PerkinElmer single-photon counting module, and at 1550 nm we use an Id Quantique detector. The connections of the two systems at different frequencies were a challenge that we were able to solve. The experimental results obtained are very well explained with the quantum analysis developed. In the first set of experiments, we measured the spectral shape of a filter (Semrock) centered at 810 nm using narrowband filtering at 1550 nm. The bandwidth measured by the filter (FWHM) was 2.75 nm. This value is within the margin of error provided by the manufacturer. This experiment is an example of verifying experimental information obtained at a certain frequency band (data provided by the manufacturer) by working with the technology available at another frequency band. This is one of the *great advantages* of the methods discussed in this Project.

3. In the second set of experiments, we have designed and measured filters with arbitrary shapes, designed using a programmable filter at 1550 nm. The shape of the filters was measured using a monochromator centered at 810 nm. The shape of the filters and the different levels of attenuation were successfully retrieved. These experiments show the versatility of the method considered and the possibilities that arbitrary spectral shaping offers for spectroscopy at any frequency band, where key optical elements might not exist.

4. We have made a full quantum analysis in the Heisenberg picture of two configurations (described in Chapters 3 and 4) for absorption spectroscopy. People use more often the Schrodinger picture in combination with a first-order approximation on the strength of the interaction (the parametric gain G). Although this approach can provide a more intuitive analysis of the problem, it has limitations. For instance, it is not possible to analyze the high-parametric gain regime of parametric down-conversion, where higher photon flux can be generated. Moreover, we have obtained simple final expressions that help in the design of experiments and the interpretation of the results.

5. We have demonstrated theoretically that the use of SU(1,1) interferometers for quantum spectroscopy is a step forward compared with the spectroscopy based on the use of *direct* quantum correlations of pairs photons generated in SPDC. We have proposed three methods of how to measure the unknown spectral shape of a filter by making measurements at another frequency band. We have shown with some examples that SU(1,1) interferometers might represent a *technological advance* for doing absorption spectroscopy based on quantum light. They don't require the measurement of coincidences between frequency-entangled photons, rather they only need to measure the flux rate of photons at one wavelength, avoiding the need of detectors at both signal and idler frequencies. It was shown that filters with arbitrary shapes can be easily recovered in both the high and low parametric gains. We have shown with the derivation of simple expressions, and some examples, that in the high parametric gain regime, photon fluxes generated are higher, so measurements can be faster (shorter detection times), and the optical detectors used can show lower sensitivity.

References

[1] M. W. Jackson, *Spectrum of belief: Joseph von Fraunhofer and the craft of precision optics*, Mit Press (2000).

[2] N. C. Thomas, "The early history of spectroscopy," *J. Chem. Educ.* **68**, 631 (1991).

[3] M. Nitzan, A. Romem, and R. Koppel, "Pulse oximetry: fundamentals and technology update," *Med. Devices: Evid.*, 231–239 (2014).

[4] G. Gauglitz, D. S. Moore, et al., *Handbook of spectroscopy*, Wiley-Vch Weinheim **1** (2014).

[5] P. Blake, E. Hill, A. Castro Neto, K. Novoselov, D. Jiang, R. Yang, T. Booth, and A. Geim, "Making graphene visible," *Appl. Phys. Lett.* **91** (2007).

[6] A. Zettner and D. Seligson, "Application of atomic absorption spectrophotometry in the determination of calcium in serum," *Clin. Chem.* **10**, 869–890 (1964).

[7] B. H. Stuart, *Infrared spectroscopy: fundamentals and applications*, John Wiley & Sons (2004).

[8] G. Scarcelli, A. Valencia, S. Gompers, and Y. Shih, "Remote spectral measurements using entangled photons," *Appl. Phys. Lett.* **83**, 5560–5562 (2003).

[9] A. Yabushita and T. Kobayashi, "Spectroscopy by frequency-entangled photon pairs," *Phys. Rev. A* **69**, 013806 (2004).

[10] A. Kalachev, D. Kalashnikov, A. Kalinkin, T. Mitrofanova, A. Shkalikov, and V. Samartsev, "Biphoton spectroscopy in a strongly nondegenerate regime of SPDC," *Laser Phys. Lett.* **5**, 600–602 (2008).

[11] O. Slattery, L. Ma, P. Kuo, Y.-S. Kim, and X. Tang, "Frequency correlated biphoton spectroscopy using tunable upconversion detector," *Laser Phys. Lett.*, **10**, 075201 (2013).

[12] G. B. Lemos, V. Borish, G. D. Cole, S. Ramelow, R. Lapkiewicz, and A. Zeilinger, "Quantum imaging with undetected photons," *Nature* **512**, 409–412 (2014).

[13] X. Zou, L. J. Wang, and L. Mandel, "Induced coherence and indistinguishability in optical interference," *Phys. Rev. Lett.* **67**, 318 (1991).

[14] X. Zou, T. Grayson, and L. Mandel, "Observation of quantum interference effects in the frequency domain," *Phys. Rev. Lett.* **69**, 3041 (1992).

[15] B. Yurke, S. L. McCall, and J. R. Klauder, "SU(2) and SU(1,1) interferometers," *Phys. Rev. A* **33** (1986).

[16] A. Hochrainer, M. Lahiri, M. Erhard, M. Krenn, and A. Zeilinger, “Quantum indistinguishability by path identity and with undetected photons,” *Rev. Mod. Phys.* **94**, 025007 (2022).

[17] Gerard J. Machado, Gaetano Frascella, Juan P. Torres, and Maria V. Chekhova, "Optical coherence tomography with a nonlinear interferometer in the high parametric gain regime," *Appl. Phys. Lett.* **117**, 094002 (2020).

[18] D. A. Kalashnikov, A. V. Paterova, S. P. Kulik, and L. A. Krivitsky, “Infrared spectroscopy with visible light,” *Nature Photonics* **10**, 98–101 (2016).

[19] R. W. Boyd, A. L. Gaeta, and E. Giese, *Nonlinear optics*, Springer, 1097–1110 (2008).

[20] Juan P. Torres, K. Banaszek, and I. A. Walmsley, "Engineering Nonlinear Optic Sources of Photonic Entanglement," *Progress in Optics* **56**, 227 (2011).

[21] J. Armstrong, N. Bloembergen, J. Ducuing, and P. S. Pershan, “Interactions between light waves in a nonlinear dielectric,” *Phys. Rev.* **127**, 1918 (1962).

[22] V. G. Dmitriev, G. G. Gurzadyan, and D. N. Nikogosyan, *Handbook of nonlinear optical crystals*, Springer **64** (2013).

[23] E. A. Ortega, J. Fuenzalida, M. Selimovic, K. Dovzhik, L. Achatz, S. Wengerowsky, R. F. Shiozaki, S. P. Neumann, M. Bohmann, and R. Ursin, “Spatial and spectral characterization of photon pairs at telecommunication wavelengths from type-0 spontaneous parametric downconversion,” *JOSA B* **40**, 165–171 (2023).

[24] R. Loudon, *Quantum Theory of Light*, Oxford University Presss, 3rd edition (2000).

[25] J. K. Blow, R. Loudon, J. D. Simon Phoenix, and T . J. Shepherd, "Continuum fields in quantum optics," *Phys. Rev. A* **42**, 4102 (1990).

[26] S. M. Barnett and P. M. Radmore, *Methods in theoretical quantum optics*, Oxford University Press (2002).

[27] B. Dayan, "Theory of two-photon interactions with broadband down-converted light and entangled photons," *Phys. Rev. A* **76**, 043813 (2007).

[28] E. Brambilla, A. Gatti, M. Bache, and L. A. Lugiato, "Simultaneous near-field and far-field spatial quantum correlations in the high-gain regime of parametric down-conversion," *Phys. Rev. A* **69**, 023802 (2004).

[29] M. I. Kolobov ed. *Quantum imaging*, Springer, 113-139 (2007).

[30] E. Brambilla, A. Gatti, M. Bache, and L. A . Lugiato, "Simultaneous near-field and far-field spatial quantum correlations in the high-gain regime of parametric down-conversion," *Phys. Rev. A* **69**, 023802 (2004).

[31] Wojciech Wasilewski, A. I. Lvovsky, Konrad Banaszek, and Czeslaw Radzewicz, "Pulsed squeezed light: Simultaneous squeezing of multiple modes," *Phys. Rev. A* **73**, 063819 (2006).

[32] R.W. Boyd, G. S. Agarwal, K.W. C. Chan, A. K. Jha, and M. N. O'Sullivan, "Propagation of quantum states of light through absorbing and amplifying media," *Opt. Commun.* **281**, 3732 (2008).

[33] R. J. Glauber, "The quantum theory of optical coherence," *Phys. Rev.* **130**, 2529 (1963).

[34] L. Mandel and E. Wolf, *Optical coherence and quantum optics*, Cambridge university press (1995).

[35] I.S. Gradshteyn and I.M. Ryzhik, *Table of integrals, series and products*, Elsevier Academic Press, Seventh Edition (2007).

[36] M. Chekhova and Z. Ou, "Nonlinear interferometers in quantum optics," *Adv. Opt. Photonics* **8**, 104–155, (2016).

[37] H. A. Haus, *Electromagnetic noise and quantum optical measurements*, Springer Science & Business Media (2000).

[38] G. B. Lemos, M. Lahiri, S. Ramelow, R. Lapkiewicz, and W. N. Plick, "Quantum imaging and metrology with undetected photons: tutorial," *JOSA B* **39**, 2200–2228 (2022).

[39] Adam Vallés, Gerard Jiménez, Salazar-Serrano, Luis José, and Juan P . Torres, "Optical sectioning in induced coherence tomography with frequency-entangled photons," *Phys. Rev. A* **97**, 023824 (2018).

[40] J. Flórez, J. S. Lundeen, and M. V. Chekhova, "Pump depletion in parametric downconversion with low pump energies," *Opt. Lett.* **45**, 4264–4267 (2020).

[41] K. Y. Spasibko, T. S. Iskhakov, and M. V. Chekhova, "Spectral properties of high-gain parametric down-conversion," *Opt. Express* **20**, 7507–7515 (2012).

[42] M. Hendrych, S. Xiaojuan, A. Valencia, and Juan P . Torres, "Broadening the bandwidth of entangled photons: A step towards the generation of extremely short biphotons," *Phys. Rev. A* **79** 023817 (2009).

[43] C. Zhang, H. Yun-Feng, L. Bi-Heng, L. Chuan-Feng, and G. Guang-Can, "Spontaneous parametric down-conversion sources for multiphoton experiments," *Adv. Quantum Technol.* **4**, 2000132 (2021).

[44] S. Parker, S. Bose, and MB. Plenio, "Entanglement quantification and purification in continuous-variable systems," *Phys. Rev. A* **61**, 032305 (2000)

[45] D. Bouwmeester, and A. Zeilinger, *The physics of quantum information: basic concepts*, Springer, 1-14 (2000).

[46] T. Pittman, YH Shih, DV Strekalov, and Alexander V Sergienko, "Optical imaging by means of two-photon quantum entanglement," *Phys. Rev. A* **52**, R3429 (1995).

[47] ZY Ou, and L Mandel, "Violation of Bell's inequality and classical probability in a two-photon correlation experiment," *Phys. Rev. Lett.* **61**, 50 (1998).

Absorption spectroscopy with quantum light

Alejandra Padilla Camargo

In the present master's thesis, we demonstrate how quantum light can be used for spectroscopy. We propose two schemes that allow one to use advanced filtering technology at one frequency band (Telecomm window around 1550 nm) to perform high-resolution frequency measurements at another frequency band (810 nm) where this technology is not commercially available.

In the first scheme we show, in a proof of concept experiment, that this can be achieved by measuring the coincidences between highly frequency-entangled signal/idler photon pairs generated via spontaneous parametric down-conversion (SPDC). We performed two measurements, in the first one we measured the spectral shape of a filter (Semrock) centered at 810 nm using a narrowband filter at 1550 nm. The bandwidth measured by the filter (FWHM) was 2.75 nm, which is within the margin of error provided by the manufacturer. In the second measurement, we designed and measured filters with arbitrary shapes, designed using a programmable filter at 1550 nm. The shape of the filters was measured using a monochromator centered at 810 nm. The shape of the filters and the different levels of attenuation were successfully retrieved. These experiments show the versatility of the method considered and the possibilities that arbitrary spectral shaping offers for spectroscopy at any frequency band, where key optical elements might not exist.

Notwithstanding, the heart of the first scheme is the measurement of coincidences between signal and idler photons for which good optical detectors (sensitive enough) at both frequency bands are fundamental. The second scheme considered avoids this limitation and allows doing absorption spectroscopy at the idler wavelength range without making any measurement at this wavelength. All measurements are made at the signal wavelength range where advanced technology exists. The key element of this second scheme is a SU(1,1) interferometer. In the second part of the project, we demonstrate theoretically that the use of SU(1,1) interferometers for quantum spectroscopy is a step forward compared with spectroscopy based on the use of direct quantum correlations of pairs photons generated in SPDC. We showed that filters with arbitrary shapes can be easily recovered in both the high and low parametric gains. We showed, with the derivation of simple expressions and some examples, that in the high parametric gain regime, the photon fluxes generated are higher, so measurements can be faster (shorter detection times), and the optical detectors used can show lower sensitivity.

7 Material properties of Lithium Niobate

This appendix describes the dependence on wavelength and temperature of the refractive index of interest of the nonlinear crystal used in this Project (a periodically poled LN crystal (PPLN) from Covesion, with lengths $L = 1$ mm and $L = 5$ mm)

7.1 Sellmeier equation

The temperature dependent refractive index is described by the Sellmeier equation (Data is provided by Covesion):

$$n(\lambda)^2 = a_1 + b_1 f + \frac{a_2 + b_2 f}{\lambda^2 - (a_3 + b_3 f)^2} + \frac{a_4 + b_4 f}{\lambda^2 - a_5^2} - a_6 \lambda^2 \tag{58}$$

where $f = (T - 24.5°C)(T - 24.5°C)$ and T is the temperature of the crystal in ºC. The following table gives the values of all coefficients:

Parameters	
a_1	5.756
a_2	0.0983
a_3	0.2020
a_4	189.32
a_5	12.52
a_6	1.32e-2
b_1	2.860e-6
b_2	4.700e-8
b_3	6.113e-8
b_4	1.516e-4

Table A.1: Sellmeier coefficients.

We evaluate the Sellmeier equation for a PPLN crystal at $T = 125.5C$, the temperature used in experiments. The refractive index for $\lambda_p = 532$ nm, $\lambda_s = 1550$ nm, and $\lambda_i = 180$ nm are:

$$\begin{aligned} n_p &= 2.2578 \\ n_s &= 2.1617 \\ n_i &= 2.1984 \end{aligned} \tag{59}$$

The inverse group velocities, D_s and D_i, of down-converted photons are:

$$\begin{aligned} D_s = (\partial k/\partial \omega_s) &= 7.3583 \times 10^{-9}\, s/m \\ D_i = (\partial k/\partial \omega_i) &= 7.6231 \times 10^{-9}\, s/m \end{aligned} \tag{60}$$

7.2 Temperature dependence of the refractive index

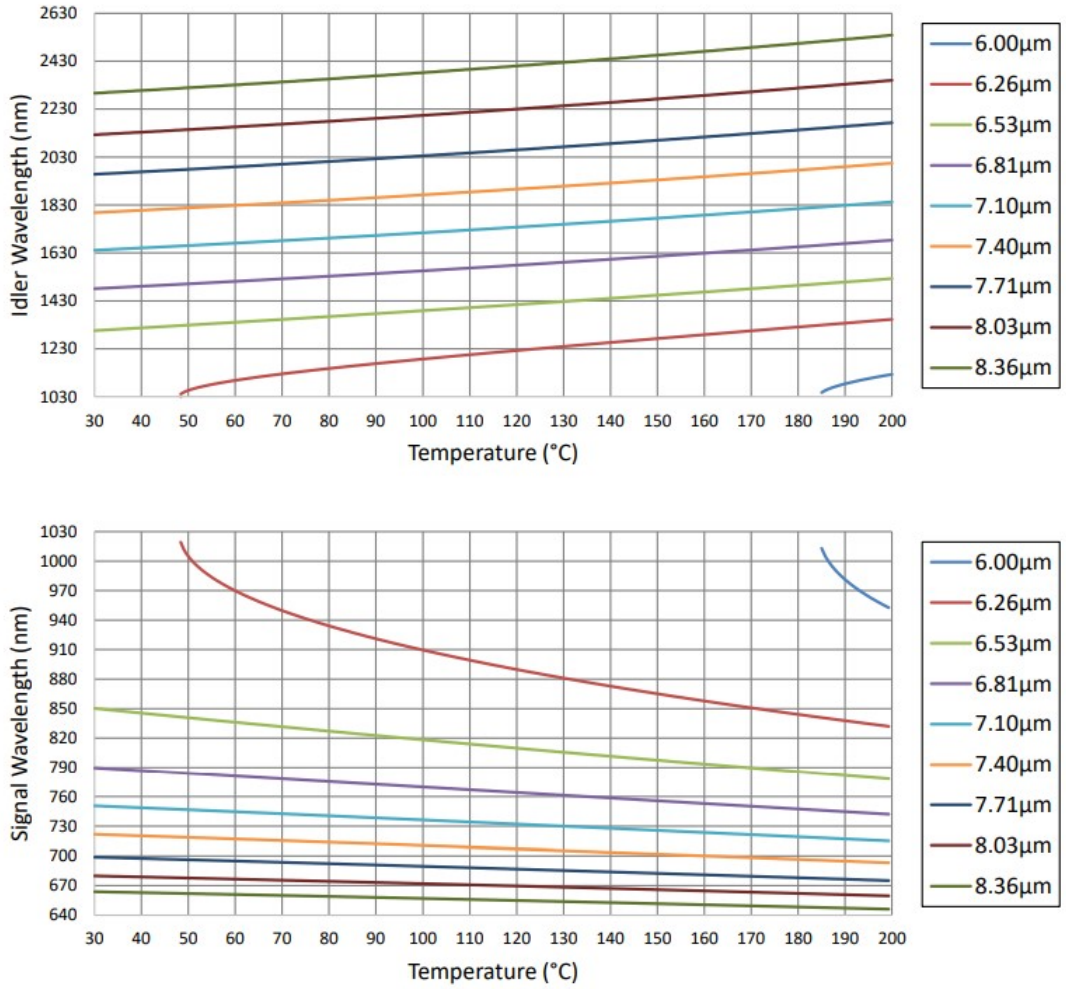

Figure. 10 Tuning curves for a Lithium Niobate crystal pump with a 515 nm pump beam. Figure obtained from Covesion.

Figure 10 shows how the emission wavelengths for the signal and idler beams change depending on the temperature of the nonlinear crystal. This data is for a 515 nm pump beam (Figure obtained from Covesion). We use this plot as a reference for a 532 nm pump beam as well. The curves corresponds to each of the 9 periodically poled gratings present in the crystal, each with a specific grating period.

8 Finisar operation principle

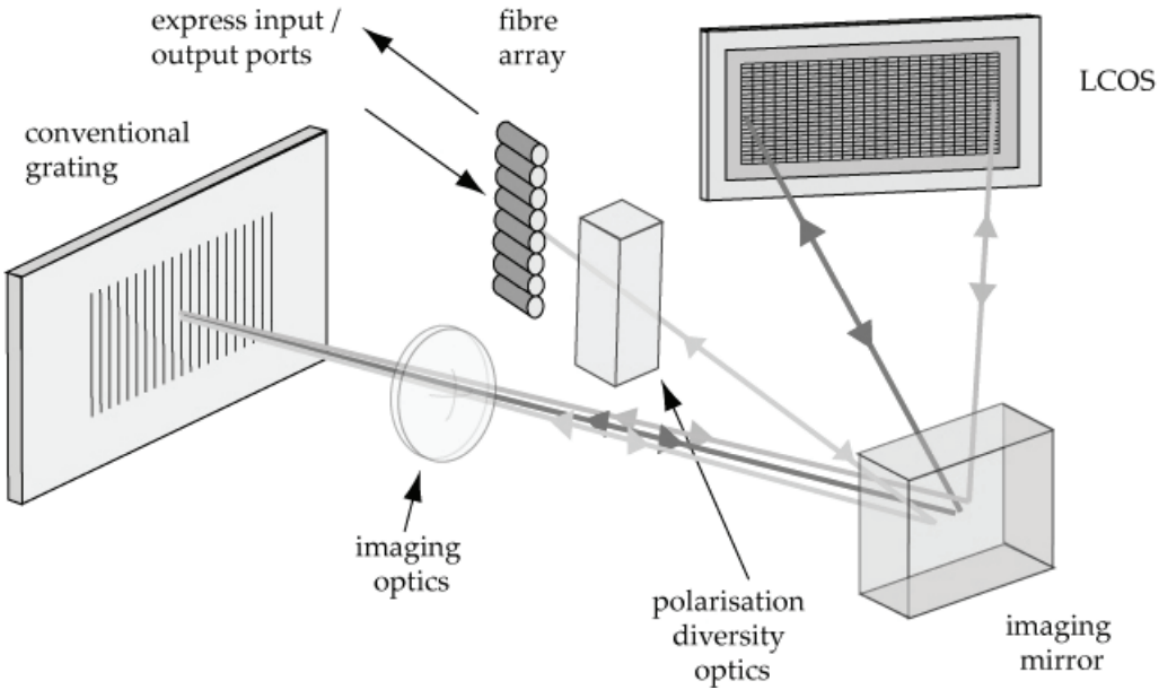

Figure. 11 Schematic of the optical design of the LCoS-based Programmable Optical Processor. Figure taken from the *WaveShaper User Manual*.

This appendix describes the principle of operation of the programmable filter (Waveshaper1000s, Finisar) used in this project (for more details see the WaveShaper User Manual).

The Waveshaper is based on Liquid Crystal on Silicon (LCoS) technology. As shown schematically in Fig. 11, light enters the device from a fiber array, then it passes through polarisation diversity optics to align orthogonal polarisation states to maximize efficiency at the diffraction grating. The grating disperses the light to the LCoS array, where the reflected light is traced back through the system to the chosen output fiber, based on the beam-steering image programmed on the LCoS array. As the wavelengths are separated on the LCoS, the control of each wavelength is independent of all others and can be switched or filtered without interfering with other wavelengths.

9 Monochromator setup and characterization.

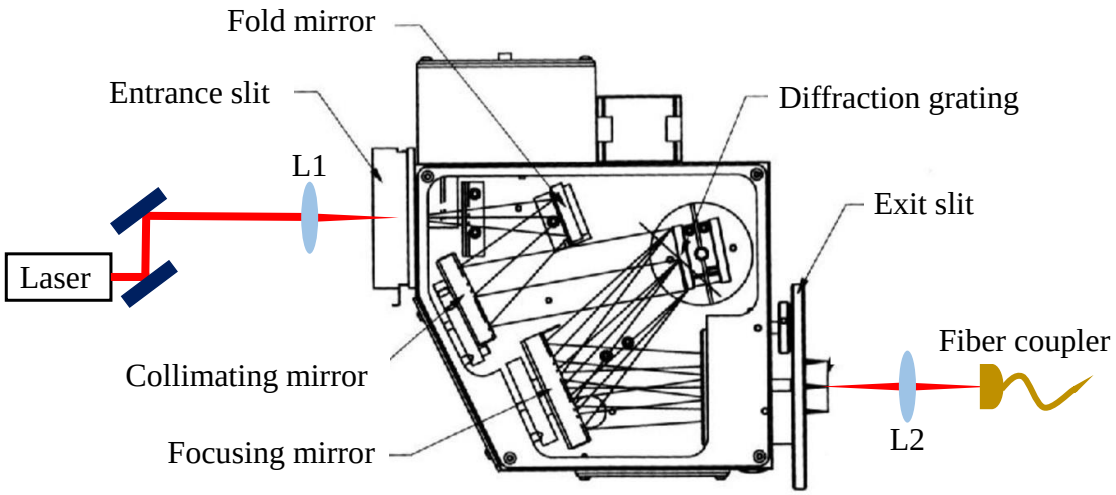

Figure. 12 Optical Design of the monochromator (MicroHR, Horiba). Figure taken from *MicroHR automated imaging spectrometer manual*.

Figure 12 shows a schematic diagram of the monochromator used in this project (for further details see the MicroHR automated imaging spectrometer manual). Light is focused into the monochromator by a lens (L1) with focal distance of $f = 5\ cm$. After passing through the entrance slit, the light is collimated and directed to a diffraction grating that is coupled to a motorized rotation stage. By rotating the grating, a spectral scan can be performed between 200 and 1100 nm with steps of 0.05 nm. The light that is reflected by the diffraction grating is sent to a mirror that focuses the light into the exit slit. Light that comes out from the exit slit is focused by a second lens (L2) with focal distance $f = 5\ cm$ and coupled into a multi mode fiber. The monochromator was calibrated prior to each measurement using a HgAr lamo (StellarNet Inc).

The bandwidth of the output spectrum from the monochromator was measured using the protocol described in Chapter 3. The idler photons, at 810 nm, were transmitted through the monochromator, which was centered at 810 nm. The output light from the monochromator was coupled to a single photon counting module (Perkin Elmer, SPCM-AQRH). The programmable filter was tuned from 1535 to 1565 and at each point the coincidences between signal and idler photons were measured. The measured coincidences spectrum is shown in Fig. 13. A Gaussian fit (solid line) was used to estimate the full-width half maximum (FWHM) of he monochromator's spectrum, which is 1.06 nm.

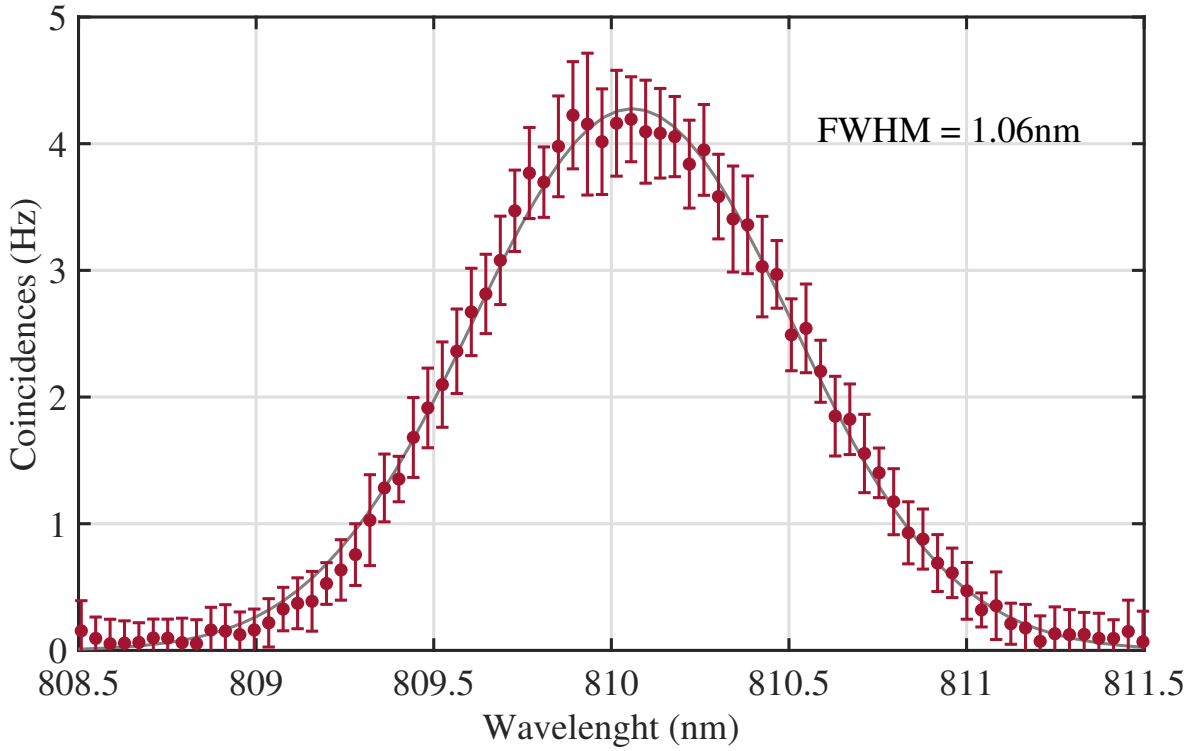

Figure. 13 Monochromator's bandwidth. Red dots correspond to the experimental data and the solid line is a Gaussian fit used to calculate the FWHM of the spectrum.

10 Origin of the term SU(1,1) interferometer

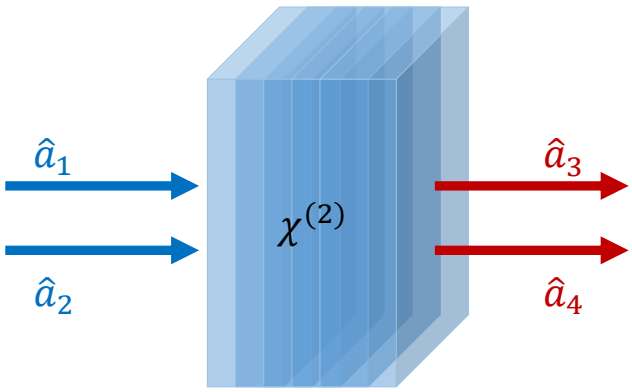

Figure. 14 Schematic illustration of a parametric down-conversion source. Input quantum operators (blue): $\hat{a}_1$ and $\hat{a}_2$; Output quantum operators (red): $\hat{a}_3$ and $\hat{a}_4$

We make the analysis in the single-mode approximation. The Bogoliuvov relationship between the input quantum operators $\hat{a}_1$ and $\hat{a}_2$, and output quantum operators. $\hat{a}_3$ and $\hat{a}_4$, as illustrated in Fig. 14, is

$$\begin{aligned} \hat{a}_3 &= U\hat{a}_1 + V\hat{a}_2^\dagger \\ \hat{a}_4 &= U\hat{a}_2 + V\hat{a}_1^\dagger \end{aligned} \tag{61}$$

where U and V are complex functions. These equations can be written in matrix form as

$$\begin{pmatrix} \hat{a}_3 \\ \hat{a}_4^\dagger \end{pmatrix} = \mathcal{T} \begin{pmatrix} \hat{a}_1 \\ \hat{a}_2^\dagger \end{pmatrix} = \begin{pmatrix} U & V \\ V^* & U^* \end{pmatrix} \begin{pmatrix} \hat{a}_1 \\ \hat{a}_2^\dagger \end{pmatrix} \tag{62}$$

A matrix $\mathcal{T}$ is said to belong to the special unitary group SU(m,n) if it fulfills the condition

$$\mathcal{U}A\mathcal{U}^\dagger = A \tag{63}$$

where

$$A_{i,j} = a_i\delta_{i,j} \begin{cases} a_i = 1 & 1 \le i \le m \\ a_i = -1 & m+1 \le i \le m+n \end{cases} \tag{64}$$

The SU(1,1) group consists of 2×2 complex matrices $\mathcal{U}$ that satisfy the relation $\mathcal{U}A\mathcal{U}^\dagger = A$, with

$$A = \begin{pmatrix} 1 & 0 \\ 0 & -1 \end{pmatrix} \tag{65}$$

It can be easily checked that this is only satisfied by matrices $\mathcal{U}$ of the form

$$\mathcal{U} = \begin{pmatrix} \alpha & \beta \\ \beta^* & \alpha^* \end{pmatrix} \tag{66}$$

with $|\alpha|^2 - |\beta|^2 = 1$. The matrix $\mathcal{T}$ in Eq.(62) is equivalent to the matrix $\mathcal{U}$ with $\alpha = U$ and $\beta = V$. $\mathcal{T}$ fulfills the relationship

$$\mathcal{T} A \mathcal{T}^\dagger = \begin{pmatrix} U & V \\ V^* & U^* \end{pmatrix} \begin{pmatrix} 1 & 0 \\ 0 & -1 \end{pmatrix} \begin{pmatrix} U^* & V \\ V^* & U \end{pmatrix} = \begin{pmatrix} 1 & 0 \\ 0 & -1 \end{pmatrix} = A \tag{67}$$

The matrix $\mathcal{T}$ that characterizes the input-output relationship between operators of a PDC source belongs to the SU(1,1) group, giving name to this Yurke-type nonlinear interferometer.